ACS OMEGA

Open Access

http://pubs.acs.org/journal/acsodf

Article

Escaping from Flatland: 3D Carborane-Based Bioisosteres of Erlotinib as Potential Anticancer Agents

Belén Dávila,[‡] Pablo Vignolo,[‡] Ignacio González, Nicole Lecot, Jenner N. Bonanata, María Fernanda García, Gustavo A. Echeverría, Oscar E. Piro, Hugo Cerecetto, and Marcos Couto*

Cite This: *ACS Omega* 2025, 10, 50468−50487

Read Online

ACCESS | Metrics & More | Article Recommendations | Supporting Information

ABSTRACT: Phenyl rings are present in nearly 45% of approved small-molecule drugs; however, their flat, aromatic nature can lead to poor solubility, metabolic instability, and limited target selectivity. Carboranes, as three-dimensional boron-rich bioisosteres, may offer a promising alternative to address these limitations. Here, we report the design, synthesis, and biological characterization of novel carborane-based analogs of erlotinib, exploring 3D bioisosterism to enhance anticancer activity. All the carborane-based analogs displayed better *in vitro* biological behavior than the parent compound, with the *para*-derivatives (**13**) and (**17**) emerging as promising leads, showing 2.5 to >12-fold greater cytotoxicity than erlotinib and up to ∼7-fold selectivities for glioblastoma over astrocytes. Compound (**17**) moderately inhibited both wild-type EGFR (IC_{50} = 9.23 μM) and the drug-resistant $EGFR_{T790M}$ mutant (IC_{50} = 7.19 μM). Molecular docking and dynamics simulations predicted binding within the ATP catalytic site, displaying a hinge-binding mode characteristic of EGFR inhibitors. Mechanistic studies revealed apoptosis as the predominant cell death pathway. *In vivo*, compound (**17**) showed excellent acute oral safety (LD_{50} > 2000 mg/kg in mice) with no alterations in biochemical blood parameters. Ames testing indicated no mutagenic potential. *In silico* ADMET profiling predicted high intestinal absorption, absence of P-gp interaction, weak hERG inhibition, and no carcinogenicity, with only compounds (**16**) and (**17**) predicted to cross the blood−brain barrier. Chemical stability assays demonstrated that all compounds, except (**18**), were stable for 24 h under physiologically relevant pH conditions (2.0, 7.0, and 8.6). Overall, these findings position compound (**17**) as a promising lead for glioblastoma tumors. Despite modest biochemical potency, its strong cellular efficacy suggests additional mechanisms of action beyond direct EGFR inhibition. Future efforts will focus on kinome-wide profiling and transcriptomic analyses to elucidate its broader target spectrum and optimize this scaffold for clinical translation.

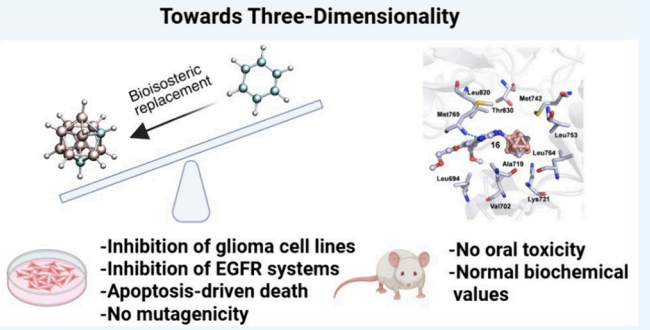

INTRODUCTION

Bioisosterism is a key strategy in medicinal chemistry that involves replacing specific atoms or functional groups within a molecule to improve its pharmacological properties while preserving biological activity.[1,2] This approach is widely used to enhance the potency, selectivity, and pharmacokinetic profiles of drug candidates. Phenyl rings, present in approximately 45% of marketed small-molecule drugs, are common pharmacophores in medicinal chemistry.[3,4] However, their planar geometry can limit molecular properties, leading to challenges such as poor aqueous solubility due to $\pi-\pi$ stacking interactions, reduced bioavailability, and metabolic liabilities.[5,6] The introduction of nonclassical three-dimensional (3D) bioisosteres offers a solution by expanding molecular topology into three-dimensional space.[7] These 3D bioisosteres can enhance solubility, disrupting crystal lattice packing, and improving solvation effects, ultimately leading to better pharmacokinetic and ADMET (absorption, distribution, metabolism, excretion, and toxicity) profiles.

The growing focus on 3D molecular structures is driven by challenges in modern drug discovery. Pharmaceutical and agrochemical industries are increasingly seeking new molecular entities, yet the discovery of such entities has declined over the past decade due to factors such as safety regulations, healthcare costs, and high clinical trial failure rates.[8] A major factor contributing to this trend is the prevalence of quasi-planar molecules within the drug discovery pipeline. Brown and Boström have demonstrated that the majority of drug-like compounds are restricted to specific regions of the chemical space, predominantly characterized by rod- or disc-shaped

Received: August 8, 2025
Revised: September 25, 2025
Accepted: October 1, 2025
Published: October 14, 2025

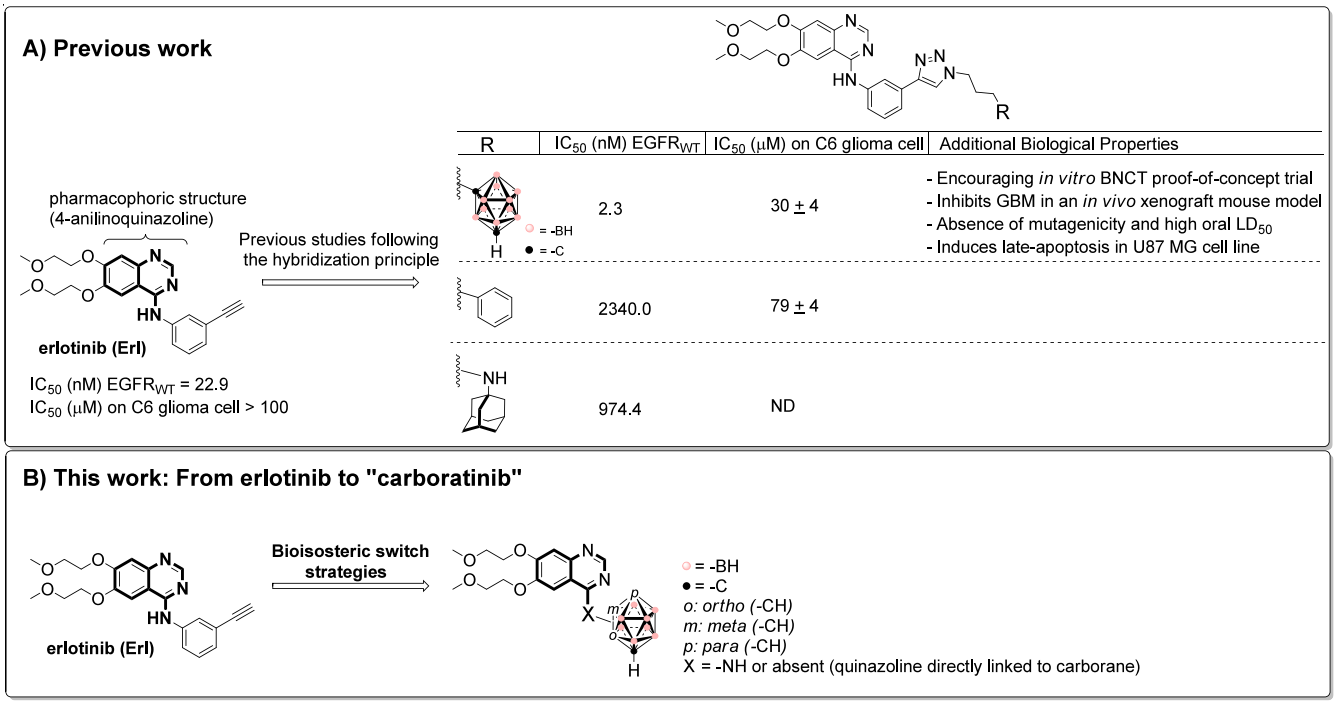

Figure 1. (**A**) *Closo*-carboranyl clusters conforming hybrid agents derived from erlotinib, acting as TKR inhibitor-scaffold, previously developed by our group.[24−28] (**B**) Rationale for the design of new carborane-based anticancer agents through the nonclassical bioisosteric replacement of the 2D aromatic ring with the 3D aromatic system.

structures, while relatively few occupy regions that favor three-dimensional molecular architectures.[9]

Nonaromatic 3D bioisosteres, such as adamantane and other saturated skeletons, including bicyclo[1.1.1]pentane, cubane, and bicyclo[2.2.2]octane, offer rigid, compact structures that can modulate molecular interactions with biological targets.[10] These 3D isosteres lack the aromaticity of phenyl rings but compensate with enhanced molecular rigidity and potential metabolic stability, making them valuable in drug design, particularly where structural stability and potency are crucial. Similarly, a distinct class of 3D bioisosteres, aromatic boron-rich clusters such as carboranes offer unique advantages.[11−14] These boron-rich clusters represent a scarcely explored yet highly promising class of nonclassical 3D bioisosteres. Composed of CH and BH vertices, these polyhedral structures exhibit remarkable properties, including high lipophilicity and the ability to form unconventional dihydrogen bonds (B−H···H−X, where X = N, O, or C).[15] Their unique geometry and electronic structure have been associated with a potential for increased metabolic stability, as no enzymes are currently known to process such motifs. The most studied variant, *closo*-dicarbadodecaborane ($C_2B_{10}H_{12}$), adopts an icosahedral geometry, where the positioning of the two carbon atoms can vary. Like benzene substitution, this variability gives rise to three distinct isomers: (1,2)-*ortho*, (1,7)-*meta*, and (1,12)-*para*, classified based on the spatial separation between the carbon atoms. This arrangement creates a robust network of multi-electron, multicenter bonds, forming a three-dimensional σ-aromatic molecule with exceptional thermodynamic and chemical stability. Notably, their size, 40% larger than the phenyl ring rotation envelope, enhances hydrophobic interactions and facilitates the crossing of the blood-brain barrier (BBB), a critical factor in treating central nervous system (CNS) diseases.[16] These unique properties make carboranes ideal candidates for drug design, particularly where increased molecular complexity and enhanced target interactions are desired.

Glioblastoma (GBM) is one of the most aggressive and prevalent primary brain tumors, presenting a formidable challenge in clinical oncology. Despite advancements in treatment strategies, including surgical resection, radiotherapy, and chemotherapy, GBM remains associated with poor prognosis, with a median survival rate of less than 15 months postdiagnosis.[17] The epidermal growth factor receptor (EGFR) is frequently overexpressed and/or mutated in various cancers, including GBM, where it plays a key role in tumor progression by promoting cell proliferation, invasion, angiogenesis, and resistance to therapy.[18] Consequently, EGFR has become a major target for small-molecule inhibitors aimed at disrupting oncogenic signaling pathways. Erlotinib (**Erl**), a well-established EGFR tyrosine kinase inhibitor (TKI), has been extensively studied in preclinical and clinical settings for GBM treatment.[19−23] In previous work, we employed a hybridization strategy by integrating the 4-anilinoquinazoline pharmacophore of **Erl** with boron-rich scaffolds such as *closo*-carbaboranes (carboranes, Figure 1).[24−28] The rational in this approach was to enhance **Erl**'s potency, selectivity, and dual applicability as both an EGFR inhibitor and generate candidates for boron neutron capture therapy (BNCT). Building on this hypothesis, the present study explores a nonclassical bioisosteric switch, replacing the *meta*-ethynylphenylamino moiety of **Erl** with various dicarboranyl isomers, including 2- and 9-amino-dicarboranyl derivatives, with the aim of expanding the molecular scaffold into 3D space to enable novel target interactions (Figure 1). We designed, synthesized, and fully biological characterized a series of carborane-based **Erl** analogs. Their biological evaluation included: (i) antiproliferative assays in three glioma cell lines with elevated EGFR expression; (ii)

https://doi.org/10.1021/acsomega.5c07982
ACS Omega 2025, 10, 50468−50487

Scheme 1. Synthesis of Bioisosteric Carboratinib Derivatives[a]

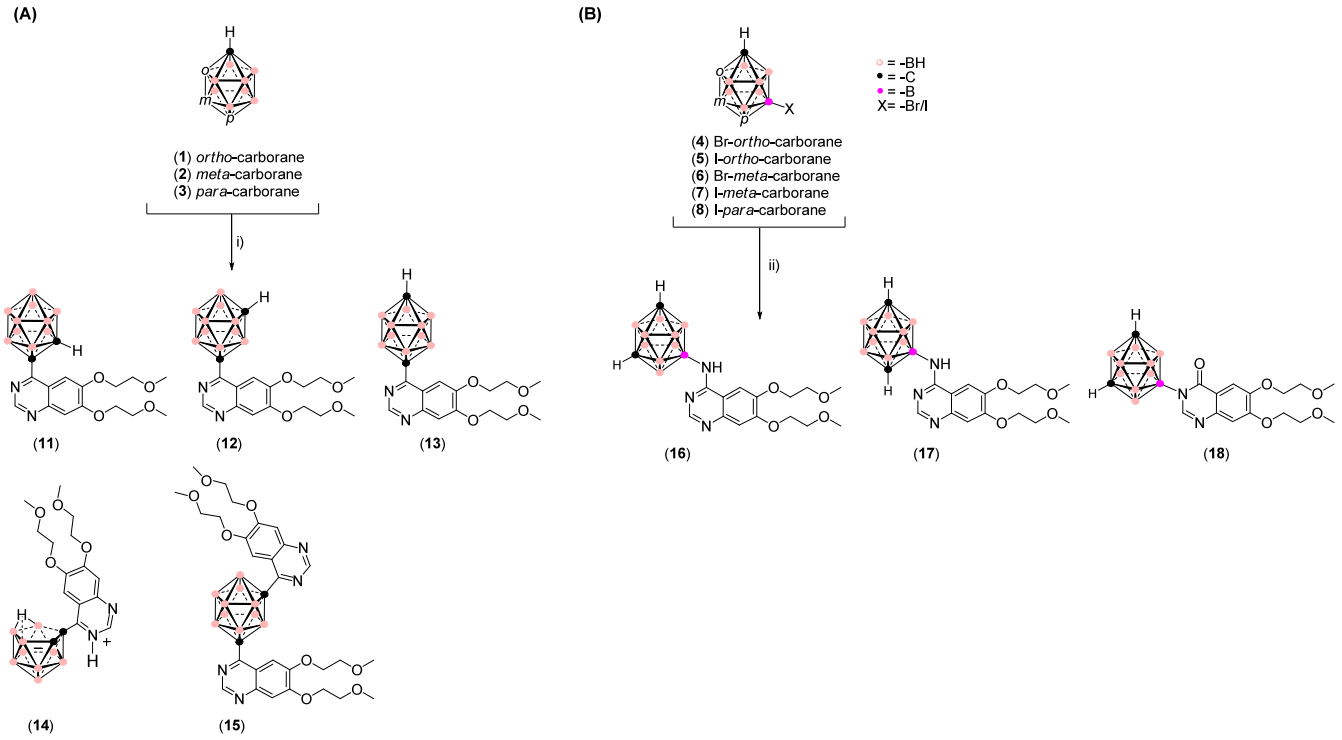

[a]**A**) Via $C_{Cluster}$−C coupling: (i) 4-chloro-6,7-bis(2-methoxyethoxy)quinazoline + *n*-BuLi in 1,2-dimethoxyethane form 0 °C to reflux, 2 h; **B**) Via B−N coupling: (ii) (**9**) or (**10**) + SPhosPdG4−SPhos−KO*t*-Bu or $Pd(dba)_2$−BINAP−KO*t*-Bu as catalyst in 1,4-dioxane, 80-95 °C for 2-24 h.

Scheme 2. Synthetic Strategy for Intermediates[a]

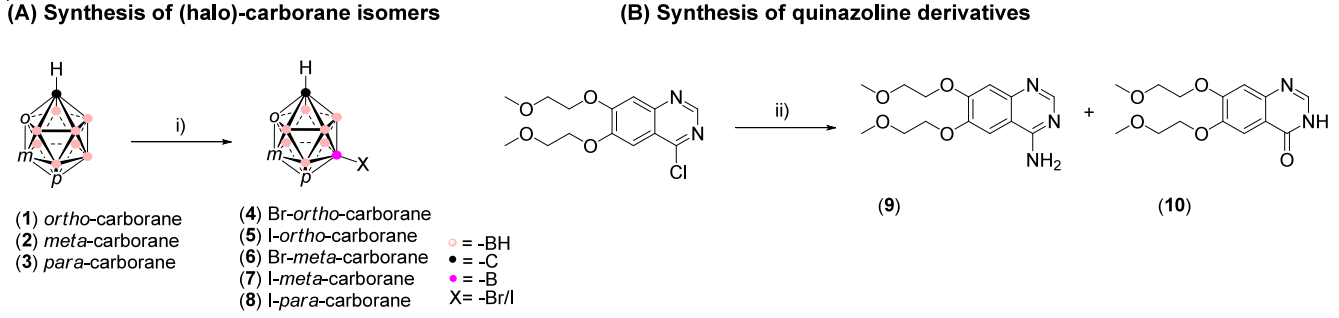

[a](**A**) Halo-carborane derivatives and (**B**) quinazoline derivatives. (i) Halogenation of the clusters; for iodination: 0,5 equiv of I_2, mixture of HNO_3/H_2SO_4 (1:1, v/v) in glacial acetic acid, 60−80 °C for 1−4.5 h, 64-90%; for bromination: 0,5/1 equiv. Br_2, mixture of HNO_3/H_2SO_4 (1:1, v/v) in glacial acetic acid, 60−80 °C for 1 h, and (ii) amination of 4-chloro-6,7-bis(2-methoxyethoxy)quinazoline; NH_4OH (25-30%), DMF, 20 °C for 40 h.

enzymatic inhibition studies against EGFR and its drug-resistant T790 M variant; (iii) molecular docking and dynamics simulations to investigate binding modes; (iv) mechanistic studies of cell death pathways; (v) mutagenicity testing; and vi) *in vivo* acute toxicity assessment including biochemical blood parameter analysis.

RESULTS AND DISCUSSION

Chemistry. Two synthetic routes were proposed for the synthesis of carborane-analogs of erlotinib, referred to herein as carboratinib, both starting from the commercially available 4-chloro-6,7-bis(2-methoxyethoxy)quinazoline. Initially, we aimed to replace the chlorine atom in the quinazoline substrate through a nucleophilic aromatic substitution (S_NAr) reaction (SI_01, Scheme S1). To this end, we synthesized two NH_2-functionalized *ortho*-carborane derivatives: one bearing the amino group on a carbon vertex of the cluster, compound **A**, and the other with the NH_2 moiety attached to the B3 position, compound **B** (SI_01, Scheme S1). Despite screening a range of reaction conditions (SI_01, Scheme S1), the desired products were not obtained. This outcome is likely due to the electron-withdrawing nature of the carboranyl moiety, which diminishes the nucleophilicity of the NH_2 group, and to a lesser extent, the potential steric hindrance around the chloroquinazoline moiety. To address these challenges, we adopted two alternative strategies: (1) S_NAr reactions between lithiated carborane isomers (**1**−**3**, Scheme 1) and 4-chloro-6,7-bis(2-methoxyethoxy)quinazoline, and (2) palladium-catalyzed Buchwald-Hartwig type cross-coupling reaction of intermediates (**4**−**8**) with (**9**−**10**) (Schemes 1 and 2). The first synthetic route

https://doi.org/10.1021/acsomega.5c07982
ACS Omega 2025, 10, 50468−50487

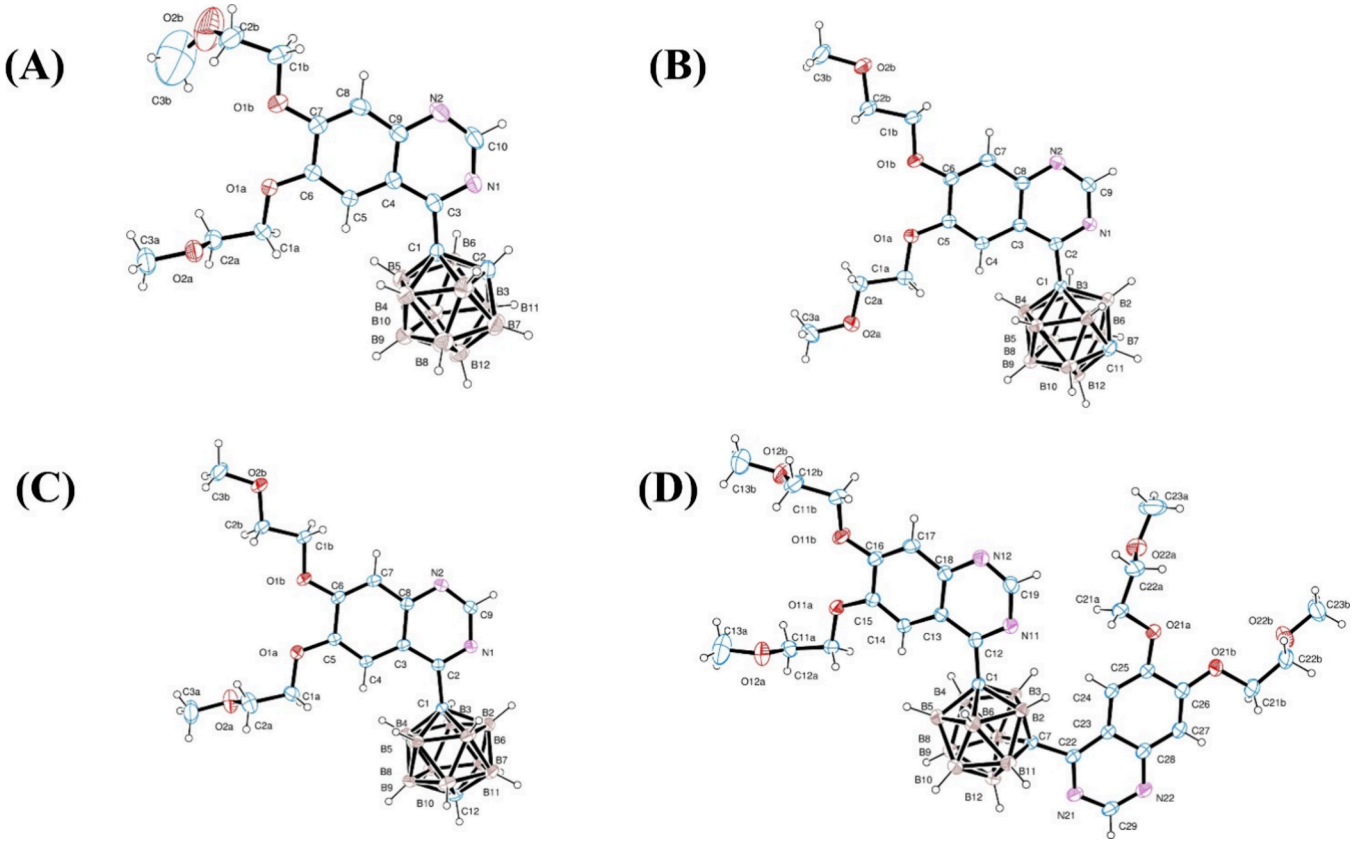

Figure 2. ORTEP plots of the solid-state structures of compounds (**11**), (**12**), (**13**), and (**15**), panels (**A**–**D**), respectively, showing the molecules in the asymmetric unit with non-hydrogen atoms labeled; displacement ellipsoids are drawn at the 30% probability level.

involved the lithiation of *ortho*-, *meta*-, or *para*-carboranyl systems using *n*-butyllithium in 1,2-dimethoxyethane, or in a mixture with tetrahydrofuran following the reaction with the chloroquinazoline. This reaction efficiently displaced the chloride atom from the quinazoline ring in each case, as illustrated in Scheme 1. The resulting products, (**11**), (**12**), and (**13**), were obtained with yields of 75%, 53%, and 57%, respectively. Recrystallization of compound (**11**) from methanol unexpectedly yielded the deboronated *nido*-derivative (**14**). Additionally, the disubstituted derivative (**15**) was obtained as a byproduct during the synthesis of compound (**12**) and was isolated in 25% yield. All derivatives were fully characterized by proton, carbon, and boron-NMR spectroscopy, mass spectrometry, HPLC, melting point, and elemental analysis (Supporting Information). Derivatives (**11**), (**12**), (**13**), and (**15**) were successfully obtained as single crystals by slow diffusion/evaporation in acetone or CH_2Cl_2/MeOH/*n*-hexane, and these crystals were suitable for X-ray diffraction analysis. The crystallographic data are provided below and in the Supporting Information. Multiple attempts to grow (**14**) single crystals suitable for X-ray diffraction were unsuccessful, as the crystals lacked the quality required for publication-grade data.

The second synthetic route employed palladium-catalyzed Buchwald-Hartwig cross-coupling reactions between 9-halo-carboranes (**4**-**8**) and the amino-quinazoline (**9**) or quinazolinone (**10**) (Scheme 2). The former were prepared by acid catalyzed halogenation (Scheme 2A) following the procedure as reported in the literature, and yielding the corresponding halo-carboranes as expected.[29,30] The compound (**9**) was obtained by *ipso* substitution of chloride by ammonia through classic S_NAr with ammonium hydroxide (NH_4OH) in DMF (77% yield), with (**10**) as a byproduct (22% yield) (Scheme 2B). Couplings between carboranes and quinazolines were performed following slightly modified procedures from those reported by Hey-Hawkins et al. for similar systems (Scheme 1B). For compound (**16**), the B–N bond was formed using the corresponding bromo-carborane with SPhosPdG4–SPhos–KO*t*-Bu as catalytic system, with a yield of 94%.[31] When using the iodo-carborane and the third generation Buchwald precatalyst, compound (**16**) was obtained in only 24% yield. Compound (**17**) was prepared with the iodo-carborane and $Pd(dba)_2$–BINAP–KO*t*-Bu, in 75% yield.[29] Finally, since lactams are known to undergo *N*-arylation under Buchwald–Hartwig cross-coupling conditions, we selected the secondary amide (compound **10**, Scheme 2) as a substrate for this transformation. Consequently, for (**18**) (Scheme 1) we tried the SPhosPdG4–SPhos–KO*t*-Bu system with the bromo-carborane and quinazolinone (**10**), and the product was isolated with a yield of only 1%. We also followed the procedures described by Hey-Hawkins et *al. to* try to generate the *ortho*- isomer coupling product, although without success. It was reported that 2-aminobenzonitrile reacted with 9-bromo-*ortho*-carborane using SPhosPdG3-SPhos- K_3PO_4 with a 30% yield of the coupling product,[29] and that 1,3-dihydro-2H-indolin-2-one coupled with 9-iodo-*ortho*-carborane using SPhosPdG4-KO*t*-Bu (without additional SPhos) with 58% yield.[32] However, no reaction was observed when quinazoline **9** was used.

Solid State Structure of (11), (12), (13) and (15). Single crystals suitable for X-ray crystallographic analysis of compounds (**11**), (**12**), (**13**), and (**15**) were obtained by slow evaporation of acetone for compound (**11**), and by evaporating a mixture of dichloromethane, methanol, and *n*-hexane (6:2:2)

https://doi.org/10.1021/acsomega.5c07982
ACS Omega 2025, 10, 50468–50487

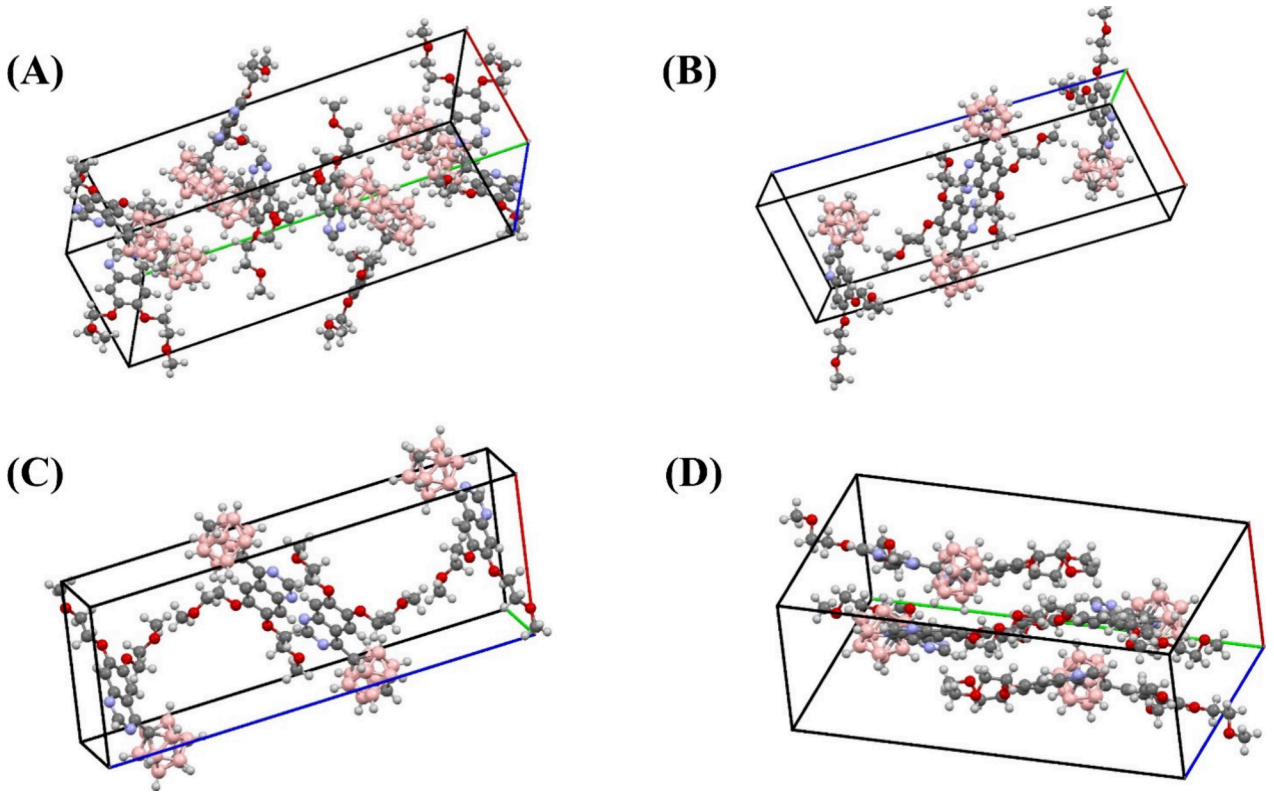

Figure 3. Unit cell contents and crystal packing arrangement for compounds (**11**), (**12**), (**13**), and (**15**), panels (**A**−**D**), respectively, as visualized using the packing tool.

for compounds (**12**), (**13**), and (**15**). The molecular structures were determined by single-crystal X-ray diffraction (Figures 2 and 3) and are consistent with the NMR data. Experimental crystal data and structure refinement parameters for all structures reported in this work are listed in Table 1. Bond lengths and angles of the studied derivatives agree with the established metrics of them. The attached *closo*-dicarbadodecaborane conforms to a slightly distorted regular icosahedron of a double carbon-substituted boron cluster. Boron and the two substituting carbon atoms are at the 12 vertices of the icosahedron, whose 30 edges constitute B−B, B−C and C−C (in the *ortho*) chemical bonds. For example, within the carbon-substituted boron clusters, B−B, Clink-B and Csust-B bond lengths are respectively in the 1.740(4)-1.791(6), 1.708(5)-1.749(3) and 1.686(6)-1.716(4) Å ranges and *ortho* C−C bond lengths in (**11**) are 1.648(4) and 1.643(4) Å. In average, X-ray diffraction results show the d(C−C) < d(Csust-B) < d(Clink-B) < d(B−B) relation among the cluster bond lengths. Tables of fractional coordinates and equivalent isotropic displacement parameters of the non-H atoms of compounds (**11**)-(**13**) and (**15**) (SI_01, Tables S2_1a-d), full bond lengths and angles (SI_01, Tables S2_2a-d), atomic anisotropic displacement parameters (SI_01, Tables S2_3a-d), hydrogen atoms positions (SI_01, Tables S2_4a-d), torsion bond angles (SI_01, Tables S2_5a-d), and H-bond distances and angles (SI_01, Tables S2_6a-d).

Crystalline materials are governed by specific intermolecular forces that stabilize the crystal structure and ensure a unique three-dimensional molecular arrangement. Hirshfeld analysis effectively characterizes these forces within the lattice. Figure 4A displays different Hirshfeld surfaces, including d_{norm}, shape index, and curvedness maps for compound (**13**), while Figure S32, SI_01 shows the corresponding maps for compounds (**12**), (**13**), and (**15**). The Hirshfeld fingerprint plot, in addition to providing a clear representation of the dominant intermolecular interactions, allows for a precise quantitative evaluation of the contribution of each individual contact within the crystal structure. As an example, the analysis for derivative (**13**), based on both fingerprint plots and d_{norm} maps, is shown in Figures 4B and C, with similar analyses for the other derivatives provided in Figure S33−S35 of the SI_01. For all derivatives, the major interactions are H···H, H···C, and O···H, with contributions of approximately 70%, 10%, and 10%, respectively. It is worth noting that the contacts observed in the dnorm map include H···H, O···H, and C···O interactions. For instance, for derivative (**13**) the H12···H3A3 contact (2.391 Å) is the shortest hydrogen−hydrogen interaction. The O2A···H12 contact (2.491 Å) highlights a hydrogen−oxygen interaction, while the C3A···O2A contact (3.175 Å) is a weaker van der Waals interaction. Most of the Length-VdW values are negative, indicating that the measured distances are slightly shorter than the expected van der Waals radii, suggesting stronger interactions. For example, the H9C···O2B contact (2.438 Å) with a Length-VdW of −0.282 indicates a stronger-than-usual interaction. These results emphasize the significance of hydrogen−hydrogen and hydrogen−oxygen interactions in stabilizing the molecular structure. The major interactions for compounds (**11**), (**12**), and (**15**) are presented in the Supporting Information.

***In Vitro* Cytotoxicity Screening.** The cytotoxicity of all synthesized compounds (**11**)-(**18**) was evaluated using sulforhodamine B assays against three different glioma cell lines: U87 MG (human), and C6 and F98 (rat), which were selected to represent varying EGFR expression backgrounds.

https://doi.org/10.1021/acsomega.5c07982
ACS Omega 2025, 10, 50468−50487

Table 1. Crystal Data and Refinement Details for Structures of Compounds 11), (12), (13) and (15)

compound	(11)	(12)	(13)	(15)
empirical formula	C_{16} H_{28} B_{10} N_2 O_4	C_{16} H_{28} B_{10} N_2 O_4	C_{16} H_{28} B_{10} N_2 O_4	C_{30} H_{44} B_{10} N_4 O_8
formula weight	420.50	420.50	420.50	696.79
temperature (K)	297(2)	297(2)	297(2)	297(2)
wavelength (Å)	0.71073	0.71073	0.71073	0.71073
crystal system	monoclinic	monoclinic	monoclinic	monoclinic
space group	$P\,2_1/c$	$P\,2_1/n$	$P\,2_1/c$	$P\,2_1/c$
unit cell dimensions				
a (Å)	11.3257(4)	10.9781(5)	11.2963(6)	9.3947(3)
b (Å)	33.011(1)	6.6430(4)	6.7249(4)	29.1473(9)
c (Å)	12.6714(4)	31.218(2)	30.462(2)	13.5888(4)
β	90.241(3)	94.577(5)	96.339(5)	103.035(3)
volume (Å^3)	4737.4(3)	2269.4(2)	2300.0(2)	3625.1(2)
Z	8	4	4	4
ρ calc. (mg mm^{-3})	1.179	1.231	1.214	1.277
μ (mm^{-1})	0.074	0.077	0.076	0.086
$F(000)$	1760	880	880	1464
crystal size (mm^3)	0.494 × 0.134 × 0.082	0.520 × 0.334 × 0.069	0.552 × 0.445 × 0.220	0.683 × 0.560 × 0.226
θ-range for data collection (°)	2.946 to 29.024	3.136 to 29.018	3.075 to 29.119	3.059 to 28.968
index ranges	$-14 \le h \le 15$	$-14 \le h \le 12$	$-14 \le h \le 15$	$-12 \le h \le 10$
	$-44 \le k \le 42$	$-8 \le k \le 8$	$-8 \le k \le 9$	$-37 \le k \le 38$
	$-17 \le l \le 15$	$-42 \le l \le 35$	$-40 \le l \le 41$	$-18 \le l \le 17$
reflections collected	58004	11541	11049	18028
independent reflections	11,140 [R(int) = 0.0845]	5035 [R(int) = 0.0401]	5095 [R(int) = 0.0320]	7937 [R(int) = 0.0264]
obs. reflections [$I > 2\sigma(I)$]	5760	3054	3532	5280
completeness (%)	99.8 (to θ = 25.242°)	99.8 (to θ = 25.242°)	99.8 (to θ = 25.242°)	99.8 (to θ = 25.242°)
data/restraints/parameters	11,140/2/666	5035/0/335	5095/0/335	7937/0/513
goodness-of-fit on F^2	1.009	1.000	1.039	1.030
final R indexes[a] [$I > 2\sigma(I)$]	R1 = 0.0782,	R1 = 0.0604,	R1 = 0.0636,	R1 = 0.0607,
	wR2 = 0.1898	wR2 = 0.1382	wR2 = 0.1574	wR2 = 0.1522
largest diff. peak/hole (e Å^{-3})	0.318/−0.250	0.209/−0.203	0.494/−0.340	0.434/−0.334

[a] $R_1 = \Sigma||F_o|-|F_c||/\Sigma|F_o|$, $wR_2 = [\Sigma w(|F_o|^2-|F_c|^2)^2/\Sigma w(|F_o|^2)^2]^{1/2}$.

U87 MG and C6 exhibit detectable endogenous EGFR expression, while F98 displays low expression levels.[24,33−35] To assess the selectivity of these compounds toward tumor cells, additional cytotoxicity assays were performed on normal cells, which consisted of a mixed population of astrocytes and oligodendrocytes. The results are summarized in Table 2. All compounds exhibited moderate to good cytotoxic activity against glioma cells and comparing to **Erl**, with IC_{50} values in the low micromolar range. Notably, the compounds, except (**18**) in some cell lines, demonstrated superior potency than the parent compound **Erl**, which exhibited an IC_{50} value of 63 μM against the U87 MG cell line and >100 μM against the F98 and C6 cell lines. Among the compounds, (**13**) and (**17**) displayed the highest cytotoxicities against U87 MG cells, (**12**), (**13**), (**15**) and (**17**) against F98 cells, and (**11**) and (**17**) against C6 cells, with IC_{50} values ranging from 8.50 μM to 25.4 μM. Compound **17** exhibited the most potent effect (IC_{50} = 8.50 μM) in C6 cells, followed by compound (**11**) (IC_{50} = 11.6 μM). In contrast, compounds (**14**) and (**15**) showed poor cytotoxicity, compared with the rest of the developed compounds, with IC_{50} values exceeding 100 μM in some cases. Notably, compound (**18**) synthesized via *N*-lactam Buchwald-Hartwig type cross-coupling reaction, exhibited a pronounced reduction in cytotoxicity against glioblastoma cell lines. This decline in activity may be attributed to the absence of the quinazoline pharmacophore, which likely plays a pivotal role in the antiproliferative effect. Regarding cellular selectivity, compounds (**11**), (**15**), and (**17**) demonstrated the most favorable SI values. Compound (**11**) displayed notable selectivity in C6 cells (SI = 5.2), while (**15**) stood out in F98 (SI > 4.1) and showed selectivity in C6 (SI > 4.0). Most prominently, (**17**) exhibited consistently high SI values across all glioma cell lines, particularly in C6 (SI = 6.9) and F98 (SI = 3.8), highlighting their well-balanced profile of potency and selectivity. Though our biochemical assays confirmed EGFR inhibition, the observed discrepancy between enzymatic potency and cytotoxicity, particularly for Erlotinib in U87 cells, suggests that target engagement may not fully account for the cellular effects. This limitation could be addressed in future studies by including BaF3 kinase-dependent models or assessing EGFR autophosphorylation by Western blot. Additionally, the enhanced cytotoxicity of carborane derivatives, even at lower biochemical potency, may indicate the involvement of alternative mechanisms of action, which remain under investigation. Taken together, these findings underscore the potential of carborane substitution to modulate tumor selectivity within this scaffold, offering a promising strategy for further lead optimization.

Inhibition of EGRF. The EGFR enzymatic inhibition of compounds (**11**)-(**18**) was studied using a luminescent kinase assay that measures ADP produced during kinase activity and poly(Glu4, Tyr1) peptide substrate provided by the manufacturer (Promega, V3831). The experiments were conducted on both wild-type EGFR ($EGFR_{WT}$) and the drug-resistant $EGFR_{T790M}$ mutant (Promega, V5324), the latter of which is a resistant variant caused by the substitution of the gatekeeper

https://doi.org/10.1021/acsomega.5c07982
ACS Omega 2025, 10, 50468−50487

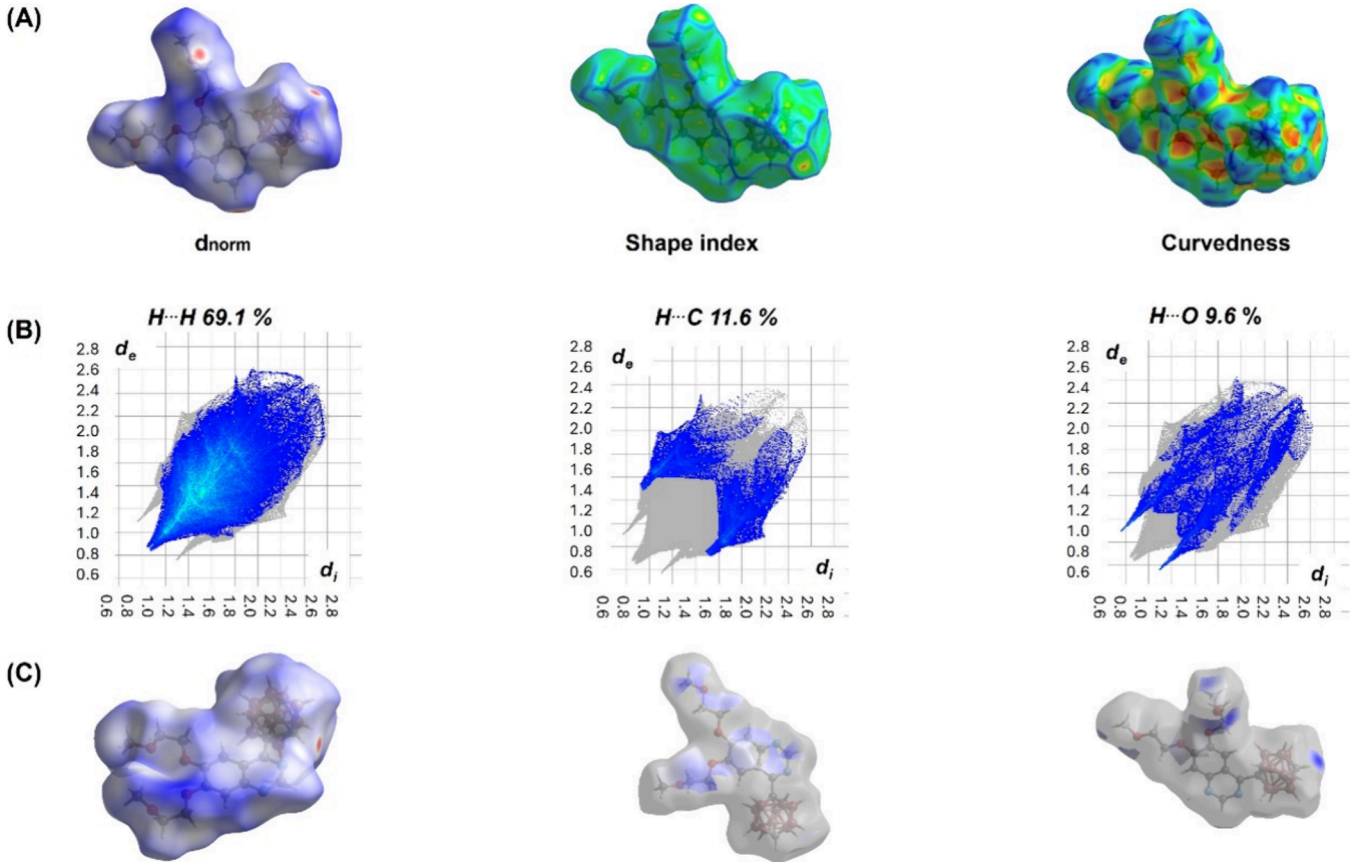

Figure 4. (A) Hirshfeld surfaces of (**13**), (B) Fingerprint plots of reciprocal short contacts in (**13**) and (C) Decomposed d_{norm} maps.

Table 2. Cytotoxicity and Selectivity of Carborane-Based Erl Analogs in Glioma and Primary Glial Cells

	cytotoxicity (IC_{50} ± SD) μM				SI[a]		
compound	U87 MG	F98	C6	mix of primary glial cell culture	U87MG	F98	C6
11	32.5 ± 3.8	54.8 ± 4.5	11.6 ± 2.3	60.4 ± 2.5	1.8	1.1	5.2
12	36.0 ± 3	24.6 ± 3.4	24.9 ± 2.1	51 ± 1	1.4	2.1	2.0
13	22.0 ± 1.5	24.2 ± 1.2	24.3 ± 1.6	50.0 ± 3.1	2.3	2.1	2.0
14	>100[c]	50.1 ± 4.9	>100[c]	>100		>2.0	
15	>100[c]	24.2 ± 2.7	24.8 ± 2.5	>100[c]		>4.1	>4.0
16	47.0 ± 1.1	75.5 ± 6.9	35.4 ± 3.2	71.2 ± 3.3	1.5	0.9	2.0
17	25.4 ± 0.7	15.6 ± 1.2	8.50 ± 0.1	58.5 ± 1.9	2.3	3.8	6.9
18	80.8 ± 9.7	116.8 ± 8.7	60.1 ± 1.1	[b]			
erlotinib	63.0 ± 5.0	>100[c]	>100[c]	>100[c]	>1.6		

[a]Selectivity index (SI) calculated as IC_{50} (primary glial cells)/IC_{50} (tumor cell line). [b]Not determined. [c]Concentrations above 100 μM could not be tested due to solubility issues. Data are presented as mean ± SD of three independent experiments obtained by sulforhodamine B assays.

threonine at position 790 with methionine (T790 M mutation) in the catalytic domain.

The reference compound erlotinib showed potent inhibition of $EGFR_{WT}$ (IC_{50} = 58 nM, Table 3), while its activity against the T790 M mutant was not measurable under our assay conditions. In contrast, osimertinib, a third-generation EGFR inhibitor clinically used to overcome T790M-mediated resistance, displayed nanomolar inhibition of the mutant enzyme (IC_{50} = 81 nM, Table 3) and no detectable activity against $EGFR_{WT}$, in line with its high selectivity. Among the carborane-based analogs, several compounds exhibited moderate to low enzymatic inhibition. The *para*-carborane derivatives **13** and **17** inhibited both EGFR variants with IC_{50} values in the low micromolar range. Notably, compound **17** displayed the most balanced profile, with IC_{50} values of 9.2 μM ($EGFR_{WT}$) and 10.4 μM ($EGFR_{T790M}$), suggesting that the presence of a *para*-carborane and an -NH linker provides comparable potency against both forms of the enzyme, Table 3. Compound **13**, which shares the same substitution pattern, also showed dual activity with similar potency. In contrast, the B−C coupled derivative **16** inhibited only $EGFR_{WT}$ (IC_{50} = 9.2 μM), but not the T790 M variant. Its amino-homologue **12** and the deboronated product **14** did not display dose−response behavior against $EGFR_{WT}$, although **14** showed weak inhibition of the mutant variant (IC_{50} = 9.6 μM). Compound **15**, bearing a different carborane connectivity, showed limited activity (IC_{50} > 5 μM) against $EGFR_{WT}$ and was inactive against the mutant. Compound **18**, which lacks the quinazoline pharmacophore, was inactive under the tested conditions, Table 3. Compound **11**, which features a quinazoline core linked to an *ortho*-

https://doi.org/10.1021/acsomega.5c07982
ACS Omega 2025, 10, 50468−50487

Table 3. Inhibitory Activity ($IC_{50} \pm SD$) of Carborane-Containing Erl Analogs against $EGFR_{WT}$ and $EGFR_{T790M}$

compound	IC_{50} (CI) μM $EGFR_{WT}$[a]	IC_{50} (CI) μM $EGFR_{T790M}$[a]
11	1.81 (0.97−3.35)	NDR[b]
12	NDR	NDR
13	12.13 (5.57−25.79)	12.31 (8.70−17.48)
14	NDR	8.73 (4.57−16.87)
15	>5.00	NDR
16	9.19 (4.32−18.59)	NDR
17	9.23 (6.18−13.85)	7.19 (4.23−12.28)
18	NDR	NDR
erlotinib	0.057 (0.050−0.087)	NDR
osimertinib	ND[c]	0.081 (0.052−0.129)

[a]The agent concentrations are those required to inhibit the phosphorylation of the poly(Glu:Tyr) substrate by 50% (IC_{50}). [b]NDR: No dose−response relationship observed within the tested concentration range. [c]ND: Not determined. CI: Confidence Interval of 95%.

carborane moiety, displayed low micromolar inhibitory activity against $EGFR_{WT}$ (IC_{50} = 1.8 μM), comparable to that of analogues **13**, **16**, and **17**. However, it failed to show a clear dose−response relationship against the $EGFR_{T790M}$ mutant, which precluded accurate determination of an IC_{50} value under the tested conditions

Notably, the enzymatic assays were performed using the T790 M single mutant, which lacks an activating mutation such as L858R. This likely limit kinase activity under assay conditions and may explain why certain compounds (e.g., **13** and **17**) displayed similar IC_{50} values for $EGFR_{WT}$ and $EGFR_{T790M}$. Future studies will include clinically relevant double mutants such as L858R/T790M.

Together, these data suggest that *para*-carborane substitution enables dual inhibition of $EGFR_{WT}$ and $EGFR_{T790M}$, whereas B−C connectivity may reduce potency and/or limit activity to the wild-type enzyme. Nonetheless, none of the tested analogs reached the potency of erlotinib or osimertinib, indicating that further optimization is required to improve kinase inhibition while retaining the unique 3D character conferred by the carborane scaffold.

Molecular Docking and Molecular Dynamic Studies on $EGFR_{wt}$. Comprehensive molecular docking simulations were performed for the inactive derivative (**12**), the active derivative (**16**) and the intermediate-active derivative (**17**) using AutoDock Vina 1.2.6, to evaluate their binding modes and interactions with the EGFR kinase domain (based on the crystal structure of the complex with erlotinib, PDB: 1M17). **Erl** was used as an internal reference ligand. For molecular dynamics simulations, the initial structures were taken either from docking poses or X-ray crystallographic data. As shown in Figure 5, all ligands bind similarly, engaging key regions of the kinase domain including the ATP-binding loop (residues 694−702), α-helix C (residues 730−745), the hinge region (residues 762−773), and the DFG motif (residues 830−833). In all compounds, the quinazoline scaffold forms a conserved hydrogen bond with the backbone NH of Met769, and hydrophobic contacts with

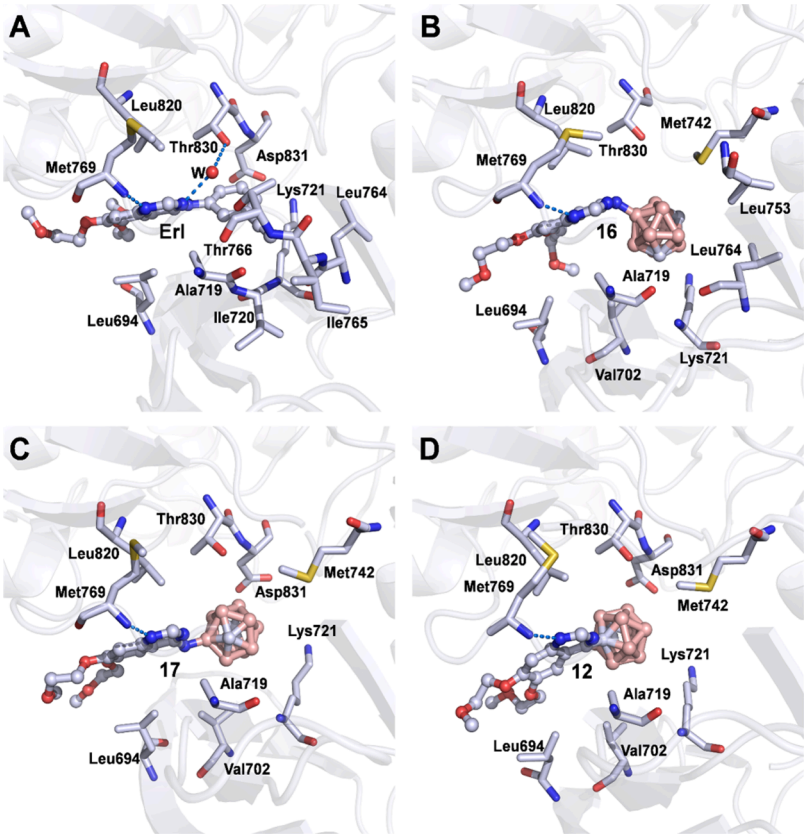

Figure 5. Ligand environment for the complexes between EGFR kinase domain and **Erl** (A), compound **16** (B), compound **17** (C) and compound **12** (D). Representative structures of the 300 ns molecular dynamics simulations were used. Figure generated with PyMOL 2.6.0a0. All compounds interact with ATP binding loop (residues 694 to 702), α-helix C (residues 730 to 745), hinge region (residues 762 to 773) and DFG motif (residues 830 to 833). Catalytic loop (residues 812 to 818) and activation loop (residues 833 to 852).

https://doi.org/10.1021/acsomega.5c07982
ACS Omega 2025, 10, 50468−50487

Leu694, Ala719, Leu768, and Leu820. In the case of **Erl**, a water-mediated hydrogen bond is also observed with Thr766, while the 3-ethynylphenyl group engages in hydrophobic interactions with the following seven residues: Ala719, Ile720, Lys721, Leu764, Ile765, Thr830, and Asp831. For compound (**16**), the *meta*-carboranyl group establishes hydrophobic interactions with the following seven residues; Val702, Ala719, Lys721, Met742, Leu753, Leu764, and Thr830. In compound (**17**), the *para*-carboranyl moiety forms contacts with the following six residues; Val702, Ala719, Lys721, Met742, Thr830, and Asp831. For (**12**), the *meta*-carboranyl group engages with the following five residues: Val702, Lys721, Met742, Thr830, and Asp831. No persistent dihydrogen bonds were observed throughout the simulations, consistent with previous findings by Kugler et al., who reported that *closo*-carboranes predominantly interact through van der Waals forces, and form only weak dihydrogen bonding.[36] In line with the number of noncovalent interactions predicted between the quinazoline moiety and amino acid residues, seven for **Erl** and (**16**), six for (**17**), and five for (**12**), it is worth noting that **Erl** and compound (**16**) establish specific contacts with Leu764, a residue located within the ATP-binding site (Figure 5). This interaction, which may contribute to ligand stabilization in the binding pocket, appears to be favored by a hinge-like conformation adopted by these molecules in the kinase domain. Such a disposition is less pronounced or absent in derivatives (**17**) and (**12**), respectively.

While molecular dynamics simulations suggest that the flexible NH linker in compound (**16**) (between the quinazoline and boron cluster) may facilitate this interaction with Leu764, enzymatic data indicate that this feature alone does not necessarily translate into enhanced inhibitory activity. In contrast, the lower activity of compound (**12**) could still be partially explained by its more compact structure, which might restrict favorable contacts at relevant concentrations.

As shown in Table 4, the estimated binding affinities vary depending on the method used. According to the MM/PBSA results, although compound (**17**) appears to exhibit the strongest predicted binding to EGFR-k, the calculated $\Delta_f G$ values for all compounds lie within the margin of error (standard deviations of 4−5 kcal·mol^{-1}), suggesting that their affinities are not significantly different Similarly, the MM/GBSA method suggests comparable affinities for **Erl** and compound (**12**), with slightly lower values for compounds (**17**) and (**16**). These discrepancies between the two methods, and their lack of correlation with experimental IC_{50} values, highlight the limitations of current free energy estimations for systems containing carborane units. It is important to note that, as previously emphasized by Sárosi and Lybrand,[76] the accuracy of carborane parameters in MM/PBSA and MM/GBSA calculations has not yet been validated.

Table 4. Summary of the Estimated Formation Free Energies ($\Delta_f G_{310}K$) for EGFR-k Complexes with Erlotinib and Compounds (12), (16), and (17) at 310 K

	$\Delta_f G_{310\ K}$ (kcal·mol^{-1})	
compound	MM/PBSA	MM/GBSA
Erl	−45 ± 5	−4 ± 5
16	−42 ± 4	−1 ± 5
17	−47 ± 4	−2 ± 5
12	−42 ± 5	−4 ± 5

Cellular Death Mechanism Studies. The cell death mechanism on U-87 MG cell line induced by compounds (**11**)-(**13**), (**16**) and (**17**) was examined using the Annexin V-Propidium Iodide (PI) double staining assay, followed by flow cytometric analysis. This technique allows for the identification of four distinct cell populations: viable cells (LL: Av^-/PI^-), early apoptotic cells (LR: Av^+/PI^-), late apoptotic cells (UR: Av^+/PI^+), and necrotic cells (UL: Av^-/PI^+). Annexin V binds to phosphatidylserine, which translocate to the outer leaflet of the plasma membrane during apoptosis, while PI serves as a marker to differentiate live cells from those that have lost membrane integrity.

As evidenced by the results (Figure 6), **Erl** induced a marked apoptotic response, with 32.6% of the cells in early apoptosis and 18.2% in late apoptosis, while only 6.15% of the population exhibited necrosis. Among the compounds evaluated, (**12**), (**13**), and (**16**) showed the highest proportion of early apoptotic cells, with percentages exceeding 40% of the cell population and less than 20% of the cells in late apoptosis. In contrast, compound (**11**) displayed an apoptotic profile very similar to that of **Erl**, with 23.2% of the cells in early apoptosis and a very similar percentage in late apoptosis, along with a notably low proportion of necrotic cells (6.86%), supporting its potential as a selective inducer of apoptosis. On the other hand, compound (**17**) exhibited the weakest pro-apoptotic effect, as reflected by the lowest percentages of early (17.6%) and late apoptotic cells (23.6%), along with some proportion of necrotic cells (9.69%). Taken together, these findings indicate that compounds (**12**), (**13**), and (**16**) effectively promote apoptosis, highlighting that compound (**16**) shows a more selective apoptotic effect. It is worth noting that compounds (**14**) and (**15**) were not included in this analysis, as their IC_{50} values exceeded 100 μM. Interesting, derivative (**17**) showed a very different cellular death mechanism profile that the parent compound and that the rest of the studied compounds being late apoptosis the main mechanism.

***In Vitro* Genetic Toxicity.** To comprehensively assess the drug development potential of compounds (**11**)-(**17**), additional toxicological evaluations were conducted, with a particular focus on key OECD guidelines for *in vitro* genetic toxicity, specifically mutagenicity.[37] The Ames test was performed using four *Salmonella* typhimurium strains (TA98, TA97, TA100, and TA1535) to evaluate the mutagenic potential of these derivatives. All tested compounds were classified as nonmutagenic, both with and without metabolic activation (Figure 7), since there was no dose-dependent increase in the number of revertant colonies and the revertant count remained below the threshold of twice the revertant-vehicle control values.

***In Vivo* Oral Acute-Toxicity and Blood Biochemical Evaluation.** To evaluate the safety profile of compound (**17**), an acute oral toxicity study was conducted in mice using the OECD Guideline 425 (Up-and-Down Procedure).[38] The compound was administered as a solution in 20% v/v DMSO, and the same vehicle was used for the control group. No mortality or adverse effects were observed at a dose of 2000 mg/kg, indicating that the LD_{50} of compound (**17**) exceeds this limit. In addition, primary behavioral and physiological observations, conducted using the Irwin test, showed no abnormal responses in treated animals compared to controls. At the end of the study, blood samples were collected for hematological and biochemical analyses (Table 5). Most serum biochemical parameters in the treated group remained within the internal and bibliographic reference ranges, including

https://doi.org/10.1021/acsomega.5c07982
ACS Omega 2025, 10, 50468−50487

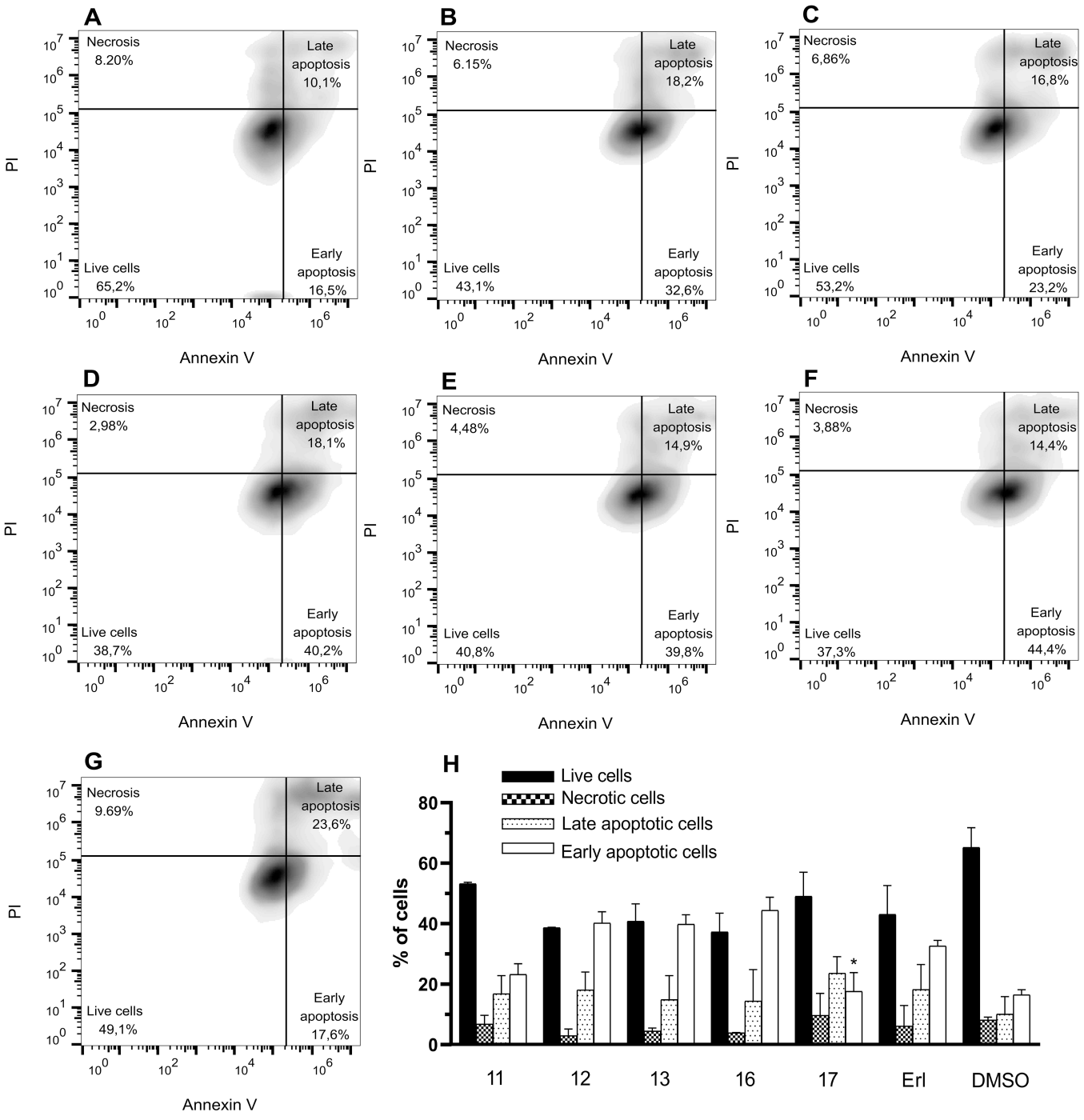

Figure 6. Phosphatidylserine exposure in U87MG cells treated with **Erl**, compounds (**11**), (**12**), (**13**), (**16**), and (**17**) at their respective IC_{50} values (Panels B–G, respectively). Cells treated with 1% DMSO served as the control (Panel A). Flow cytometry analysis was performed after 24 h of incubation. Quantitative data are shown in Panel H, as mean ± SD from three independent experiments. Statistical significance was determined using one-way ANOVA followed by Dunnett's multiple comparisons test: (*) $p < 0.02$, compared to **Erl.**.

indicators of hepatic function (ALT, ALP, total bilirubin), renal function (urea, creatinine), and electrolyte balance (Na^+, K^+, Ca^{2+}, P). A mild increase in creatinine was observed but remained within acceptable physiological variation. Notably, alanine aminotransferase (ALT) levels were lower in the treated group than in controls, further supporting the absence of hepatotoxicity Taking together, these findings indicate that compound (**17**) exhibits a low acute toxicity with no major biochemical alterations, supporting its suitability for further preclinical development.

***In Silico* ADMET Profiling and pH Stability Studies.** In the early stages of drug discovery, absorption, distribution, metabolism, excretion, and toxicity (ADMET) profiles is crucial for identifying promising drug candidates. Computational prediction of these parameters offers a valuable tool to support decision-making and prioritizing compounds before moving to more resource-intensive experimental assays. In this work, we performed *in silico* ADMET profiling representative carboratinib (derivatives **11**-**18**) using the admetQSAR toolkit[40] (Table 6),

https://doi.org/10.1021/acsomega.5c07982
ACS Omega 2025, 10, 50468−50487

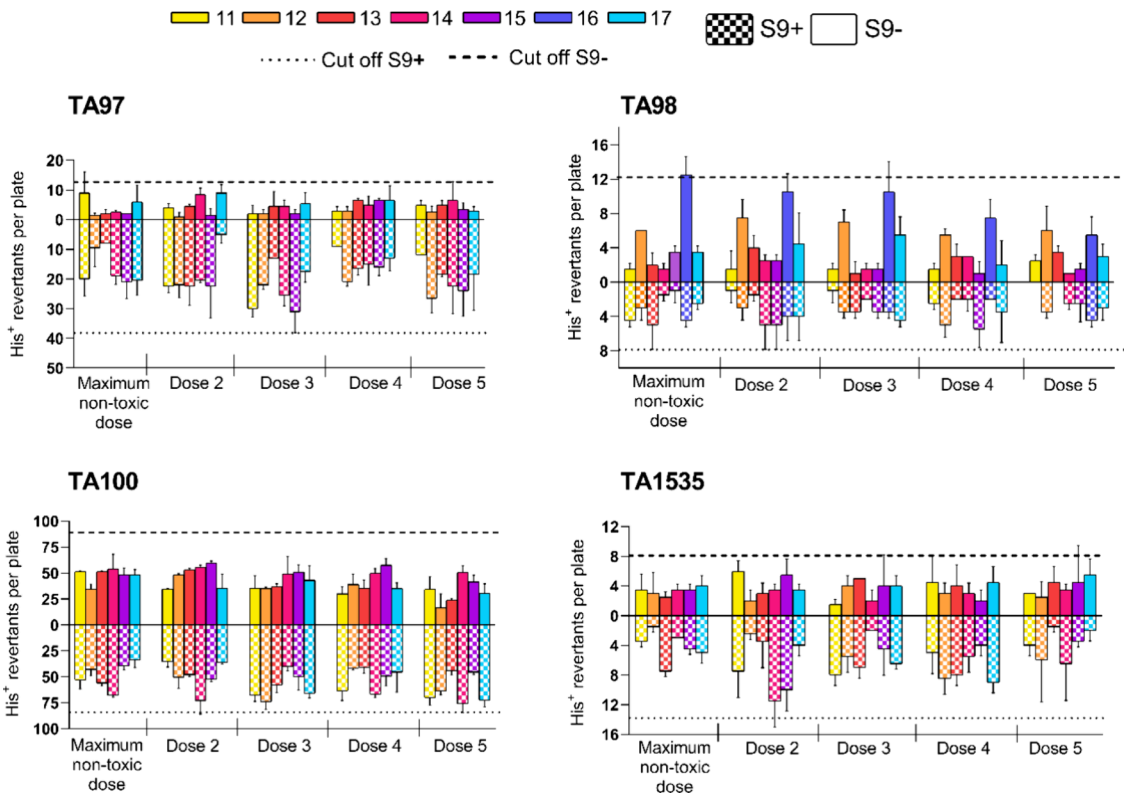

Figure 7. Ames test results for compounds (**11**)-(**17**) in S. typhimurium strains TA97, TA98, TA100, and TA1535, with ($S9^+$) and without ($S9^-$) metabolic activation. No dose-dependent increase in revertant colonies and no exceeding the threshold were observed. All compounds were classified as nonmutagenic.

Table 5. Serum Biochemical Parameters in Control and Treated Mice after Administration of Compound (17)[a]

biochemical parameters	units	control	treated mouse	internal references[b]	bibliographic references[38,39]
total protein	g/dL	4.55 ± 0.07	4.67 ± 0.05	3.6−6.6	4.9−7.3
alkaline phosphatase	U/L	145.0 ± 19.7	136.6 ± 13.5	62−209	136.3−589.5
amylase	U/L	587.5 ± 67.1	624 ± 70	200−2500	
cholesterol	mg/dL	106.0 ± 2.8	113 ± 2	36−96	81−208
glucose	mg/dL	186.5 ± 34.6	163.7 ± 11.1	63−192	85−281
creatinine	mg/dL	0.355 ± 0.007	0.54 ± 0.3	0.3−1	0.2−0.5
albumin	g/dL	2.75 ± 0.07	2.6 ± 0.2	2.5−4.8	3.1−5.3
globulins	g/dL	1.8 ± < 0.1	2.0 ± 0.3	0.5−4	1.61−5.39
total bilirubin	mg/dL	0.195 ± 0.09	0.24 ± 0.01	0.1−9	0.2−0.7
alanine aminotransferase	U/L	139.5 ± 24.7	104.3 ± 7.5	28−132	40−170
blood urea nitrogen	mg/dL	23.4 ± 0.28	24.6 ± 2.9	14−29	7−31
Ca	mg/dL	8.3 ± 0.14	8.56 ± 0.05	3.3−8.7	
P	mg/dL	7.34 ± 0.028	7.43 ± 1.55	2.3−8.7	
K	mmol/L	6.41 ± 0.69	6.86 ± 0.32	4.7−6.4	14.3−24.2
Na	mmol/L	151.5 ± 6.36	150 ± 3	126−145	298.56−394.3
total bile acids	μmol/L	13.2 ± 1.83	9.7 ± 1.8	0−15	

[a]Values are expressed as mean ± SD. [b]*Internal reference ranges* were generated by the biochemical analyzer based on the selected species and strain (BALB/c mouse). No significant alterations were observed in the treated group compared to controls.

aiming to preliminarily assess their drug-likeness and pharmacokinetic behavior.

Most compounds were predicted to have positive high human intestinal absorption (HIA), although Caco-2 permeability values suggested limited passive transcellular diffusion. All derivatives were classified as noninhibitors of P-glycoprotein (P-gp) and the renal organic cation transporter OCT2, indicating a low risk of efflux-mediated resistance and transporter-related drug−drug interactions. Regarding metabolic stability, all compounds were predicted to be substrates of CYP3A4, suggesting susceptibility to first-pass metabolism, an important consideration for oral administration. In terms of safety, weak inhibition of the hERG channel was uniformly predicted, and no carcinogenic potential was identified. Additionally, all compounds were predicted to be nonmutagenic in the Ames test (Supporting Information, SI_01), which is consistent with the experimental findings (see above). Notably, among all analogues evaluated, only compounds **16** and **17** were predicted to cross the blood-brain barrier (BBB), possibly due to the presence of an *NH* linker between the quinazoline and the carborane

https://doi.org/10.1021/acsomega.5c07982
ACS Omega 2025, 10, 50468−50487

Table 6. Drug-like Properties of 11-18 and Erl[a]

	absorption				metabolism	toxicity	
cmpd.	HIA[b]	Caco-2[c]	P-gp inh[d]	OCT2 inh[e]	CYP-subs[f]	hERG[g]	Carc[h]
11	(+)	(−)	(−)	(−)	CYP450 3A4	w-inh[45]noninh[46]	(−)
12	(+)	(−)	(−)	(−)	CYP450 3A4	w-inh[45]noninh[46]	(−)
13	(+)	(−)	(−)	(−)	CYP450 3A4	w-inh[45]noninh[46]	(−)
14	(+)	(−)	(−)	(−)	CYP450 3A4	w-inh[45]noninh[46]	(−)
15	(+)	(−)		(−)	CYP450 3A4	w-inh[45]noninh[46]	(−)
16	(+)	(−)	(−)	(−)	CYP450 3A4	w-inh[45]noninh[46]	(−)
17	(+)	(−)	(−)	(−)	CYP450 3A4	w-inh[45]noninh[46]	(−)
18	(+)	(−)	(−)	(−)	CYP450 3A4	w-inh[45]noninh[46]	(−)
Erl	(+)	(+)	(−)	(−)	CYP450 3A4	w-inh[45]noninh[46]	(−)

[a]To maintain clarity, distribution parameters are not shown in the table. Nevertheless, subcellular localization predictions consistently identified mitochondria as the primary target organelle. [b]Human intestinal absorption (HIA): if the compound has HIA% less than 30%, it is labeled as (−), otherwise it is labeled as (+).[41] [c]Caco-2 permeability. If the compound has the Caco-2 permeability value $\geq 8 \times 10^{-6}$ cm/s, it is labeled as high Caco-2 permeability (+) otherwise it is labeled as moderate−poor permeability (−).[42] [d]P-glycoprotein inhibition. Non inhibition is labeled as (−) otherwise it is labeled as (+). [e]Renal organic cation transporter (OCT2) inhibition.[43] Non inhibition is labeled as (−) otherwise it is labeled as (+). [f]Ability to be substrate of three cytochrome P450 isoenzymes (CYP4502C9, CYP4502D6 and CYP4503A4).[44] It is shown the predicted isoform-CYP that the compound potentially acts as substrate. [g]Human ether-a-go-go-related gene inhibition.[45,46] Non inhibition is labeled as 'non', weak inhibition is labeled 'w-inh' and inhibition is labeled 'inh'. [h]Potential as carcinogens.[47] Non carcinogen is labeled as (−).

moieties (Supporting Information, SI_01). This feature may be relevant when considering potential applications in CNS-targeted therapies. Overall, the ADMET profiles support the drug-likeness of the carboratinib series and are broadly comparable to those of **Erl**, in line with its known pharmacological behavior.

Additionally, experimental stability studies were conducted under physiologically relevant pH conditions (pH 2.0, 7.0, and 8.6) for compounds **11**−**18**, to evaluate their chemical robustness across the gastrointestinal environment.[48] All compounds remained chemically stable for up to 24 h under the tested conditions, except for compound **18**, which exhibited significant degradation at pH 2.0. This behavior was anticipated based on the known acid lability of the corresponding amide moiety. Representative chromatograms for all tested conditions are provided in the Supporting Information (Figure S44−S70).

CONCLUSIONS

In this study, we designed, synthesized, and physicochemical and biologically characterized a series of novel carborane-based analogs of erlotinib, employing a 3D nonclassical bioisosteric strategy aimed at enhancing anticancer activity. Among the tested compounds, the *para*-isomer (**17**) emerged as the most promising candidate, displaying up to a 12-fold increase in cytotoxicity compared to Erlotinib and improved selectivity toward glioblastoma cells over primary astrocytes, with selectivity indices ranging from 2.3 to 6.9 depending on the cell line. Compound (**17**) also exhibited moderate inhibitory activity against both wild-type EGFR (IC_{50} = 9.23 μM) and the drug-resistant $EGFR_{T790M}$ mutant (IC_{50} = 7.19 μM), the latter being a clinically relevant target for overcoming resistance to first-generation EGFR inhibitors. Molecular docking and dynamics simulations predicted binding within the ATP catalytic site, revealing a characteristic hinge-binding conformation for the most potent kinase inhibitors. Studies on the type of cell death induced by the compounds indicated that apoptosis was the predominant mechanism, with no evidence of mutagenic potential observed in the Ames test. Furthermore, compound (**17**) demonstrated a favorable acute oral toxicity profile *in vivo*, with an LD_{50} exceeding 2000 mg/kg in mice. Biochemical blood parameter analysis showed no alterations compared to vehicle-treated animals, further supporting its safety and a wide therapeutic window. *In silico* ADMET predictions further supported the drug-likeness of this series, indicating high intestinal absorption, absence of P-gp interaction, and no inhibition of OCT2. Although limited Caco-2 permeability and CYP3A4 metabolism suggest susceptibility to first-pass effects, weak hERG inhibition and lack of predicted carcinogenicity or mutagenicity reinforce a favorable safety profile. Notably, only compounds (**16**) and (**17**) were predicted to cross the blood-brain barrier (BBB), likely due to the presence of an NH linker between the quinazoline and the carborane moieties, an advantageous property for addressing brain tumors such as glioblastoma. Experimental stability assays under physiologically relevant pH conditions (2.0, 7.0, and 8.6) demonstrated that all compounds, except (**18**), were chemically stable over 24 h, supporting their potential for oral administration.

Altogether, these results suggest that compound (**17**) stands out as a promising lead for glioblastoma and drug-resistant EGFR-expressing tumors. Despite its limited biochemical potency, its pronounced cellular activity indicates the involvement of additional or alternative mechanisms of action beyond direct EGFR inhibition. To further explore its target landscape and guide rational optimization, future studies will include comprehensive kinome profiling as well as transcriptomic analyses (e.g., RNA-seq) to elucidate the pathways and molecular networks involved.

EXPERIMENTAL SECTION

Chemistry. Chemicals were reagent grade and were used as received from commercial suppliers. 1,2-*closo*-$C_2B_{10}H_{12}$, 1,7-*closo*-$C_2B_{10}H_{12}$ and 1,12-*closo*-$C_2B_{10}H_{12}$ were obtained from Zhengzhou Yuanli Biological Technology Co., Ltd., Henan, China. 4-chloro-6,7-bis(2-methoxyethoxy)quinazoline was obtained from BaoJi GuoKang Bio- Technology Co., Ltd. Baoji City, Shaanxi, China. Compounds **4**, **5**, **6**, **7**, **8** were synthesized as reported in the literature.[29,30] Most reactions were conducted under a dinitrogen atmosphere using standard Schlenk techniques. Analytical thin-layer chromatography (TLC) was performed on precoated silica gel 60 F254 plates (Merck) supported on aluminum foil. Compound visualization was

https://doi.org/10.1021/acsomega.5c07982
ACS Omega 2025, 10, 50468−50487

achieved under UV light (254 nm) or by exposure to iodine vapor in a sealed chamber. For column chromatography, silica gel 60A (0,070−0,200 mm) from Carlo Erba or aluminum oxide 90 active neutral (0,063−0,200 mm) from Merck was used. Melting points were measured on an Electrothermal 9100 apparatus and are uncorrected. Elemental analyses were performed using a Carlo Erba Model EA1108 elemental analyzer instrument. All NMR spectra were recorded on Bruker DPX-400 spectrometers equipped with the appropriate decoupling accessories. The operating frequencies were as follows: ^{1}H at 400.13 MHz, ^{11}B{^{1}H} at 128.38 MHz, and ^{13}C{^{1}H} at 100.77 MHz. NMR spectra were recorded in $CDCl_3$, CD_3COCD_3 or $(CD_3)_2SO$ at 298 K. Chemical shifts are reported in units of parts per million (ppm) downfield from the reference, and all coupling constants are reported in Hertz. Multiplicity is abbreviated as s is the singlet, d is the doublet, dd is the doublet of doublet, dt is doublet of triplets, dq is doublet of quartets, t is the triplet, m is the multiplet, and bs is the broad singlet. High-performance liquid chromatography coupled to mass spectrometry (HPLC-MS) was performed using an Ultimate 3000 system (Thermo Scientific) equipped with an autosampler and a UV−vis detector set to monitor wavelengths from 180 to 400 nm. Mass spectrometric detection was carried out on a TSQ Fortis triple quadrupole mass spectrometer (Thermo Scientific) using an OptaMax NG heated electrospray ionization (H-ESI) source. The mass range was set from m/z 5 to 3000. Theoretical mass spectra were generated using the SimulTar isotope pattern calculator (Scientific Instrument Services, https://www.sisweb.com/mstools/isotope.htm). HPLC analyses were performed on an Agilent 1200 Series Infinity Star HPLC system equipped with a UV detector. A C18 column (Restek, 10 μm, 250 × 4.5 mm) was used, with a flow rate of 1 mL/min. The mobile phase consisted of (A) water with 0.1% trifluoroacetic acid (TFA) and (B) methanol (MeOH). The gradient program was as follows: 0−10 min, 80% B; 10−30 min, 100% B; 30−32 min, 0% B. Eluted peaks were monitored at 335 nm.

Structural X-ray Diffraction. The measurements were performed on an Oxford Xcalibur, Eos, Gemini CCD diffractometer employing graphite-monochromated MoKα (λ = 0.71073 Å) radiation. X-ray diffraction intensities were collected (ω scans with ϑ and κ-offsets), integrated and scaled with CrysAlisPro suite of programs.[49] The unit cell parameters were obtained by least-squares refinement (based on the angular settings for all collected reflections with intensities larger than seven times the standard deviation of measurement errors) using CrysAlisPro.

The diffraction pattern of compound (**11**) was mainly due to a monoclinic twinned crystal featuring the contribution of a major single crystal domain and a much smaller one (about 17% of scattering power) obtained through a rotation of 180° around the reciprocal a*-axis. Because a unit cell β angle very close to 90°, the weighted reciprocal lattices showed considerable overlap with each other, hence resembling a quasi-merohedral twin. The structure was solved in the unit cell of the major single crystal domain from its perturbed diffraction data employing the dual procedure implemented in SHELXT.[50] Isotropic least-squares refinement of the non-H molecular model with SHELXL[51] showed, as expected, several anomalies due to unaccounted twinning distortion of the diffraction data, including (i) a relatively large agreement R1-factor (= 0.214); (ii) observed reflections which should be systematically absent; (iii) the most disagreeable reflections showed observed intensities (F_o^2) systematically larger than calculated (F_c^2) ones. We then proceeded to refine the molecular model treating the diffraction data as due to a quasi-merohedral twin. Now R1-factor dropped to 0.160, there were no systematic absence violations and F_o^2vs. F_c^2 much less biased. At this stage, the crystal structure showed solvent accessible voids with a total volume of 487 Å3 per unit cell and hosting 11 electrons that was interpreted as disordered solvent. We therefore undertook the further refinement of the ordered part of the structure through a procedure described in ref 52 and implemented in the SQUEEZE software included in the PLATON[53] suite of programs. As a result, the isotropic R1-factor reduced to 0.154. Following an anisotropic refinement, a difference Fourier map showed all (11) hydrogen atoms of the icosahedral carbon-substituted boron cluster and most of the remaining ones. The first group of H atoms was refined at their found locations with isotropic displacement parameters and the rest refined at their expected geometric positions (methyl groups at staggered angular conformations) with the riding model. The final R1-factor was 0.078 and the mass fraction of the minor twin equal to 0.172(1).

As for (**11**), all hydrogen atoms of the icosahedral cluster of compounds (**12**), (**13**) and (**15**) were in a different Fourier map and refined at their found positions. The rest of the H atoms were refined with the riding model, but now the angular conformation of the methyl groups was optimized by treating them as rigid groups allowed to rotate around the corresponding O−CH3 bond such as to maximize the sum of the electron density at the calculated H-positions.

Crystallographic structural data have been deposited at the Cambridge Crystallographic Data Centre (CCDC) with reference number CCDC 2457089 (**11**), 2457090 (**12**), 2457091 (**13**) and 2457092 (**15**).

Hirshfeld Surface Analysis. To analyze the intermolecular interactions present in the solid-state structures of compounds (**11**), (**12**), (**13**), and (**15**), Hirshfeld surface (HS)[54] analysis was carried out using the CrystalExplorer17.5 software.[55] The structural information was obtained directly from the experimentally determined CIF files of each crystal, while hydrogen atom positions were standardized to default bond lengths during the calculations.

For each point on the Hirshfeld surface, two distances are considered: d_i, the distance from the surface point to the nearest atom within the molecule (internal to the surface), and d_e, the distance to the closest atom outside the molecule (external to the surface). These distances are combined into a normalized contact distance (d_{norm}), calculated according to the following equation:

$$d_{norm} = \{d_i - r_i^{vdw}\}/\{r_i^{vdw}\} + \{d_e - r_e^{vdw}\}/\{r_e^{vdw}\}$$

where r_i^{vdW} and r_e^{vdW} represent the van der Waals radii of the respective atoms. Negative values of d_{norm} indicate contacts shorter than the sum of van der Waals radii, while positive values reflect longer contacts. The associated 2D fingerprint plots further assist in visualizing and quantifying the nature and relative contributions of different intermolecular contacts in the crystal packing of each compound.

General Procedure for the Synthesis of Bioisosteric Carboratinib Derivatives *via* $C_{Cluster}$−C Coupling (Compounds 11−15). Under a dinitrogen atmosphere, *n*-butyllithium (1 equiv., 0.625 mL, 1.6 mol/L in hexane) was added dropwise to a solution of *ortho*-, *meta*-, or *para*-carborane

https://doi.org/10.1021/acsomega.5c07982
ACS Omega 2025, 10, 50468−50487

(1 equiv., 150 mg, 1.0 mmol) in DME (8 mL) at 0 °C. The reaction mixture was stirred at 0 °C for 45 min. In a separate flask, a solution of 4-chloro-6,7-bis(2-methoxyethoxy)-quinazoline (1.1 mmol in 10 mL of DME) was prepared and added under an inert atmosphere to the previously cooled carboranyl-lithium solution. The resulting mixture was heated under reflux for 2 h. After completion, the reaction was quenched with saturated aqueous NH_4Cl (30 mL), transferred to a separatory funnel, and extracted with CH_2Cl_2 (3 × 15 mL). The combined organic layers were dried over anhydrous $MgSO_4$, filtered, and concentrated under reduced pressure to dryness. In all cases, any unreacted starting carborane was removed by sublimation using a coldfinger apparatus under vacuum. Compounds (**11**−**15**) were purified either by preparative thin-layer chromatography (TLC) using CH_2Cl_2:MeOH (95:5) as eluent, or by recrystallization, as detailed for each compound

General Procedure for the Synthesis of Bioisosteric Carboratinib Derivatives via *B*−*N* Coupling (Compounds 16−**18).** An oven-dried 25 mL Schlenk round-bottom two-necked flask was charged the corresponding halo-carborane (**4**-**8**), quinazoline, catalyst, ligand and base, and evacuated three times. The mixture was then suspended in anhydrous 1,4-dioxane and placed in a preheated oil bath, where it was stirred for 2−24 h at 80−95 °C. The reaction was monitored by TLC (silica gel, dichloromethane/methanol, 95:5 (v/v)). The turbid brown mixture was diluted with acetone and filtered through Celite. The solvent was evaporated and the crude oily mass was further purified via column chromatography (alumina gel, *n*-hexane/ethyl acetate, 6:4 (v/v)), yielding the products as a brown paste.

N-(*closo*-1,7-dicarbadodecaboran(12)-9-yl) −6,7-bis(2-methoxyethoxy)quinazolin-4-amine (**16**) was synthesized from **6** (69 mg, 0.31 mmol), 1.1 equiv of **9** (100 mg, 0.34 mmol), SPhosPdG4 (5 mol %, 14 mg), SPhos (5 mol %, 7 mg), and 2.0 equiv of KO*t*-Bu (77 mg, 0.69 mmol), in 0.6 mL of 1,4-dioxane. The mixture was stirred at 80 °C for 2 h. Yield 94% (127 mg, 0.29 mmol).

N-(*closo*-1,12-dicarbadodecaboran(12)-9-yl)-6,7-bis(2-methoxyethoxy)quinazolin-4-amine (**17**) was synthesized from **8** (37 mg, 0.136 mmol), 1 equiv of **9** (40 mg, 0,.36 mmol), $Pd_2(dba)_3$ (5 mol %, 16 mg), BINAP (5 mol %, 17 mg), and 1.2 equiv of KO*t*-Bu (18 mg, 0.16 mmol), in 2.5 mL of 1,4-dioxane. The mixture was stirred at 95 °C for 20 h. Yield 75% (43 mg, mmol).

N-(*closo*-1,7-dicarbadodecaboran(12)-9-yl)-6,7-bis(2-methoxyethoxy)quinazolinone (**18**) was synthesized from **6** (82 mg, 0.37 mmol), 1.1 equiv of **10** (217 mg, 74 mmol), SPhosPdG4 (5 mol %, 15 mg), SPhos (5 mol %, 8 mg), and 2.0 equiv of KO*t*-Bu (46 mg, 0.41 mmol), in 3.7 mL of 1,4-dioxane. The mixture was stirred at 80 °C for 2 h. Yield 1% (2 mg, mmol).

*Synthesis of 6,7-Bis(2-methoxyethoxy)quinazolin-4-amine (**9**) and 6,7-Bis(2-methoxyethoxy)quinazolinone (**10**).* 4-chloro-6,7-bis(2-methoxyethoxy)quinazoline (500 mg, 1.6 mmol) was suspended in a 2:1 (v/v) mixture of ammonium hydroxide 25% and dimethylformamide (12 mL) and stirred for 40 h at room temperature. The mixture was then extracted with ethyl acetate (4 × 20 mL) and the combined organic layer was washed with brine, dried over anhydrous sodium sulfate, and filtered. The solvent was evaporated under reduced pressure, and purification by column chromatography (alumina gel, dichloromethane/methanol, 97:3 (v/v)) gave **9** as a white solid (316 mg, 77%), and **10** as a yellow solid (102 mg, 22%).

Compound 9. ^{1}H NMR (400.13 MHz, $CDCl_3$) δ: 8.49 (s, 1H, pyrimidine-**H**), 7.19 (s, 1H, Ar-**H**), 7.06 (s, 1H, Ar-**H**), 5.67 (bs, 2H, N**H**$_2$), 4.28 (t, J = 4 Hz, 2H, (-C**H**$_2$-OAr)), 4.23 (t, J = 4 Hz, 2H, (-C**H**$_2$-OAr)), 3.85 (t, J = 4 Hz, 2H, (H_3CO-C**H**$_2$-), 3.82 (t, J = 4 Hz, 2H, (H_3CO-C**H**$_2$-), 3.47 (s, 6H, (**H**$_3$CO−)$_2$) ^{13}C{^{1}H}-NMR (100.77 MHz, $CDCl_3$) δ: 159.96, 155.01, 153.94, 148.73, 147.51, 108.63, 108.42, 103.43, 71.05, 70.61, 69.28, 68.43, 59.46, 59.42. Anal. Calcd For $C_{14}H_{19}N_3O_4$: C, 57.33; H, 6.53; N, 14.33. Found: C, 57.27; H, 6.48; N, 14.20.

Compound 10. ^{1}H NMR (400.13 MHz, $CDCl_3$) δ: 8.06 (, 1H, pyrimidine-**H**), 7.58 (s, 1H, Ar-**H**), 7.15 (s, 1H, Ar-**H**), 4.35−4.17 (m, 4H, (-C**H**$_2$-OAr)$_2$), 3.92−3.77 (m, 4H, (-C**H**$_2$-OAr)$_2$), 3.47 (s, 3H, (**H**$_3$CO−)), 3.47 (s, 3H,, (**H**$_3$CO−)). ^{13}C{^{1}H}-NMR (100.77 MHz, $CDCl_3$) δ: 162.40, 155.03, 148.92, 145.25, 142.57, 115.74, 109.17, 106.72, 70.69, 70.52, 68.67, 68.56, 59.35, 59.31. Anal. Calcd For $C_{14}H_{18}N_2O_5$: C, 57.13; H, 6.16; N, 9.52. Found: C, 57.17; H, 6.16; N, 9.51.

Compound 11. 4-(1,2-Dicarba-closo-dodecaboran-1-yl)-6,7-bis(2-methoxyethoxy)quinazoline

Single crystals were obtained by slow diffusion/evaporation in CH_2Cl_2/MeOH/*n*-Hexane (6:2:2).

^{1}H{^{11}B}-NMR (400.13 MHz, $CDCl_3$) δ: 8.92 (s, 1H, pyrimidine-**H**), 8.02 (s, 1H, Ar-**H**), 7. 34 (s, 1H, Ar-**H**), 5.71 (bs, 1H, -C$_{cluster}$-**H**), 4.35−4.29 (m, 4H, (-C**H**2-OAr)2), 3.89−3.87 (m, 4H, (H3CO-C**H**2-)2), 3.49 (s, 3H, (**H**$_3$CO−)), 3.48 (s, 3H, (**H**$_3$CO−)). ^{13}C{^{1}H}-NMR (100.77 MHz, $CDCl_3$) δ: 155.96, 153.78, 151.45, 150.61, 150.50, 117.36, 108.10, 104.83, 74.49, 70.53, 70.30, 68.97, 68.74, 60.26, 59.38, 59.37. ^{11}B{^{1}H}-NMR (128.38 MHz, $CDCl_3$) δ: −1.67 (1B), −2.74 (1B), −8.32 (2B), −9.90 (2B), −11.67 (2B), −13.42 (2B). HPLC-t_R = 19.81 min.; purity: 99.1% relative area. Anal. Calcd For $C_{16}H_{28}B_{10}N_2O_4$: C, 45.70; H, 6.71; N, 6.66. Found: C, 45.68; H, 6.73; N, 6.64. mp: 168−170 °C. Yellow needles in 75% yield.

Compound 12. Single crystals were obtained by slow diffusion/evaporation in CH_2Cl_2/MeOH(6:4)

4-(1,7-Dicarba-closo-dodecaboran-1-yl)-6,7-bis(2-methoxyethoxy)quinazoline

^{1}H{^{11}B}-NMR (400.13 MHz, $CDCl_3$) δ: 9.00 (s, 1H, pyrimidine-**H**), 7.94 (s, 1H, Ar-**H**), 7.29 (s, 1H, Ar-**H**), 4.29 (ddd, J = 7.3, 3.7, 2.6 Hz, 4H, (-C**H**2-OAr)2), 3.99−3.76 (m, 4H, m, 4H, (H3CO-C**H**2-)2), 3.49 (s, 3H,(**H**3CO−), 3.46 (s, 3H, (**H**3CO−), 3.33 (bs, 1H, -C$_{cluster}$-**H**). ^{13}C{^{1}H}-NMR (100.77 MHz, $CDCl_3$) δ: 155.51, 155.29, 151.79, 150.61, 149.95, 117.71, 108.24, 105.50, 78.35, 70.60, 70.34, 68.87, 68.57, 59.37, 59.33, 54.61. ^{11}B{^{1}H}-NMR (128.38 MHz, $CDCl_3$) δ: −4.58 (1B), −6.25 (1B), −10.70 (4B), −13.39 (4B). HPLC-t_R = 21.38 min.; purity: 97.5% relative area. Anal. Calcd For $C_{16}H_{28}B_{10}N_2O_4$: C, 45.70; H, 6.71; N, 6.66. Found: C, 45.69; H, 6.73; N, 6.67. mp: 86−89 °C. Pale yellow needles in 53% yield.

Compound 13. 4-(1,12-Dicarba-closo-dodecaboran-1-yl)-6,7-bis(2-methoxyethoxy)quinazoline

Single crystals were obtained by slow diffusion/evaporation in CH_2Cl_2/MeOH(6:4)

^{1}H{^{11}B}-NMR (400.13 MHz, $CDCl_3$) δ: δ 8.91 (s, 1H, pyrimidine-**H**), 7.94 (s, 1H, Ar-**H**), 7.24 (s, 1H, Ar-**H**), 4.31 (t, J = 4 Hz, 2H, (H3CO-C**H**2-)), 4.27 (t, J = 4 Hz, 2H, (H3CO-C**H**2-)), 3.89 (t, J = 4 Hz, 2H, (H3CO-C**H**2-)), 3.83 ((t, J = 4 Hz, 2H, (H3CO-C**H**2-)), 3.50 (s, 3H, (**H**3CO−), 3.44 (s, 3H, (**H**3CO−), 3.00 (bs, 1H, -C$_{cluster}$-**H**). ^{13}C{^{1}H}-NMR (100.77 MHz, $CDCl_3$) δ: 156.16, 155.00, 151.73, 150.50, 149.62, 117.18,

https://doi.org/10.1021/acsomega.5c07982
ACS Omega 2025, 10, 50468−50487

108.16, 105.81, 86.34, 70.63, 70.31, 68.83, 68.47, 64.06, 59.38, 59.29. $^{11}B\{^1H\}$-NMR (128.38 MHz, $CDCl_3$) δ: −12.84 (5B), −16.01 (5B).). HPLC-t_R = 21.38 min.; purity: 95.6% relative area. Anal. Calcd For $C_{16}H_{28}B_{10}N_2O_4$: C, 45.70; H, 6.71; N, 6.66. Found: C, 45.69; H, 6.69; N, 6.70. mp: 116−117 °C. White needles in 57% yield.

Compound 14. 6,7-Bis(2-methoxyethoxy)-4-(1H-quinazolin-1-ium-4-yl)-*nido*-7,8-$C_2B_9H_{12}$

$^1H\{^{11}B\}$-NMR (400.13 MHz, DMSO-d6) δ: 8.96 (s, 1H, pyrimidine-**H**), 7.50 (s, 1H, Ar-**H**), 7.41 (s, 1H, Ar-**H**), 5.26 (bs, NH) 3.87 (dd, J = 5.2, 3.8 Hz, 4H, (-C**H**2-OAr)2)), 3.80−3.76 (m, 4H, (-C**H**2-OAr)2)), 3.38 (s, 3H, (**H**3CO−)), 3.35 (s, 3H, (**H**3CO−)), 2.41 (bs, 1H, -$C_{cluster}$-**H**), −2.62 (bs, 1H, bridge B−H). $^{13}C\{^1H\}$-NMR (100.77 MHz, $CDCl_3$) δ: 167.74, 158.69, 150.74, 150.50, 146.34, 120.65, 119.86, 106.51, 106.31, 70.30, 70.23, 69.74, 69.30, 58.85, 58.57, 45.46. $^{11}B\{^1H\}$-NMR (128.38 MHz, $CDCl_3$) δ: −5.34 (1B), −9.54 (1B), −13.30 (2B), −16.45 (2B), −19.50 (1B), −31−44 (1B), −35.48 (1B). HPLC-t_R = 20.44 min.; purity: 99.1% relative area. Anal. Calcd For $C_{16}H_{28}B_9N_2O_4$: C, 46.91; H, 6.89; N, 6.84. Found: C, 46.88; H, 6.89; N, 6.85. mp: 279−280 °C. Orange needles in 74% yield.

Compound 15. Single crystals were obtained by slow diffusion/evaporation in CH_2Cl_2

1,7-Bis[6,7-bis(2-methoxyethoxy)quinazolin-4-yl]-1,7-dicarba-closo-dodecaborane

$^1H\{^{11}B\}$-NMR (400.13 MHz, $CDCl_3$) δ: 9.02 (s, 1H, pyrimidine-**H**), 8.08 (s, 1H, Ar-**H**), 7.32 (s, 1H, Ar-**H**), 4.37−4.25 (m, 4H, (-C**H**2-OAr)2), 3.90−3.77 (m, 4H, (-C**H**2-OAr)2), 3.54 (s, 3H, (**H**3CO−)), 3.46 (s, 3H, (**H**3CO−)). $^{13}C\{^1H\}$-NMR (100.77 MHz, $CDCl_3$) δ: 155.61(2C), 155.48 (2C), 151.58 (2C), 150.29 (2C), 150.12 (2C), 117.80 (2C), 107.96 (2C), 105.34 (2C), 77.26, 70.61, 70.40 (2C), 70.32 (2C), 68.85 (2C), 68.67 (2C), 59.44 (2C), 59.38 (2C). $^{11}B\{^1H\}$-NMR (128.38 MHz, $CDCl_3$) δ: −3.51 (2B), −10.93 (8B). HPLC-t_R = 13.26 min.; purity: 97.8% relative area. Anal. Calcd For $C_{30}H_{44}B_{10}N_4O_8$: C, 51.71; H, 6.36; N, 8.04. Found: C, 51.74; H, 6.35; N, 8.00. mp: 105−107 °C. Beige needles in 25% yield.

Compound 16. *N*-(*closo*-1,7-Dicarbadodecaboran(12)-9-yl) −6,7-bis(2-methoxyethoxy)quinazolin-4-amine

$^1H\{^{11}B\}$-NMR (400.13 MHz, $CDCl_3$) δ: 8.57 (s, 1H, pyrimidine-**H**), 7.19 (s, 1H, 1H, Ar-**H**), 7.11 (s, 1H, 1H, Ar-**H**), 5.30 (bs, 1H, N**H**), 4.32−4.18 (m, 4H, (-C**H**2-OAr)2), 3.88−3.78 (m, 4H, (-C**H**2-OAr)2), 3.47 (s, 3H, (**H**3CO−)), 3.46 (s, 3H, (**H**3CO−)), 2.90 (bs, 2H, -$C_{cluster}$-**H**). $^{13}C\{^1H\}$-NMR (100.77 MHz, $CDCl_3$) δ: 160.46, 157.85, 154.42, 153.76, 148.39, 109.57, 108.32, 103.82, 71.07, 70.52, 69.55, 68.23, 59.30, 59.27, 51.56 (2C). $^{11}B\{^1H\}$-NMR (128.38 MHz, $CDCl_3$) δ: 0.29 (1B, BN), −6.71 (2B), −11.10 (1B), −13.86 (2B), −15.65 (2B), −18.64 (1B), −22.11 (1B). HPLC-t_R = 10.76 min.; purity: 99.0% relative area. MS: m/z calcd. 435,53; found: 436,35. The observed isotopic pattern agreed with the calculated one. Anal. Calcd For $C_{16}H_{29}B_{10}N_3O_4$: C, 44.12; H, 6.71; N, 9.65. Found: C, 44.08; H, 6.72; N, 9.64. mp: 68−69 °C. White solid in 94% yield.

Compound 17. *N*-(*closo*-1,12-Dicarbadodecaboran(12)-9-yl)-6,7-bis(2-methoxyethoxy)quinazolin-4-amine

$^1H\{^{11}B\}$-NMR (400.13 MHz, $CDCl_3$) δ: 8.47 (s, 1H, pyrimidine-**H**), 7.19 (s, 1H, Ar-**H**), 7.10 (s, 1H, Ar-**H**), 5.25 (bs, 1H, NH), 4.32 (t, J = 4 Hz, 2H, (H3CO-C**H**2-)), 4.27 (t, J = 4 Hz, 2H, (H3CO-C**H**2-)), 3.86 (td, J = 4.9, 1.4 Hz, 4H, (-C**H**2-OAr)2), 3.50 (s, 3H, (**H**3CO−)), 3.47 (s, 3H, (**H**3CO−)), 2.74 (bs, 2H, -$C_{cluster}$-**H**). $^{13}C\{^1H\}$-NMR (100.77 MHz, $CDCl_3$) δ: 158.35, 152.78, 151.95, 146.84, 145.58, 109.41, 107.07, 101.51, 69.27, 68.71, 67.78, 66.44, 57.98 (2C), 57.55, 57.49. $^{11}B\{^1H\}$-NMR (128.38 MHz, $CDCl_3$) δ: −4.00 (1B), −13.33 (2B), −14.70 (3B), −15.94 (3B), −17.05 (1B). HPLC-t_R = 12.52 min.; purity: 96.9% relative area. MS: m/z calcd 435,53; found: 436.34. The observed isotopic pattern agreed with the calculated one. Anal. Calcd For $C_{16}H_{29}B_{10}N_3O_4$: C, 44.12; H, 6.71; N, 9.65. Found: C, 44.13; H, 6.69; N, 9.66. White solid in 75% yield.

Compound 18. *N*-(*closo*-1,7-Dicarbadodecaboran(12)-9-yl)-6,7-bis(2-methoxyethoxy)quinazolinone

$^1H\{^{11}B\}$-NMR (400.13 MHz, $CDCl_3$) δ: 8.01 (s, 1H, pyrimidine-**H**), 7.66 (s, 1H, Ar-**H**), 7.17 (s, 1H, Ar-**H**), 4.31−4.20 (m, 1H, (-C**H**2-OAr)2), 3.88−3.80 (m, 1H, (-C**H**2-OAr)2). 3.47 (s, 6H, ($\mathbf{H}_3$CO−)$_2$, 3.02 (bs, 2H, -$C_{cluster}$-**H**). $^{11}B\{^1H\}$-NMR (128.38 MHz, $CDCl_3$) δ: 0.21 (1B), −6.69 (2B), −11.25 (1B), −13.60 (2B), −14.90 (2B), −18.35 (1B), −20.54 (1B). HPLC-t_R = 19.78 min.; purity: 95.6% relative area. White solid in 1% yield.

BIOLOGY

***In Vitro* Cytotoxicity Assays on EGFR-Expressing Cells.** Cells from the U-87MG, C6, and F98 lines were cultured in 96-well plates (between 5,000 and 10,000 cells/well) in a final volume of 100 μL and allowed to grow for 24 h at 37 °C and 5% CO_2. Following this, 125 μL of fresh culture medium was added, and the cells were incubated for an additional 24 h to allow further growth. Subsequently, 25 μL of a 10× stock solution of the test compounds, prepared in culture medium at the desired final concentration, was added to each well. The cells were then incubated for another 24 h. After incubation, the culture medium was carefully removed, and the cells were washed twice with 200 μL of phosphate-buffered saline (PBS). Fixation was performed by adding 50 μL of ice-cold trichloroacetic acid (TCA) to each well, followed by incubation at 4 °C for 1 h. The plates were then washed five times with distilled water and left to air-dry at room temperature. Next, the fixed cells were stained with 50 μL of a 0.4% (w/v) sulphorhodamine B (SRB) solution, prepared in 1% (v/v) acetic acid. The staining process was carried out at room temperature for 30 min. After incubation, excess SRB and unbound dye were removed by rapidly washing the plates at least five times with 1% (v/v) acetic acid until no residual dye remained. The plates were then left to air-dry for a minimum of 24 h. To solubilize the protein-bound SRB, 100 μL of 10 mM Tris base buffer (pH 10) was added to each well, and the plates were gently agitated on a shaker platform for 5 min. The optical density (OD) of the resulting solution was measured at 540 nm using a 96-well plate reader. The OD of the SRB solution in each well was directly proportional to the number of viable cells. The percentage of viable cells (%CV) was calculated using the following equation:

$$\%CV = ((A540 - B)/(C - B)) \times 100$$

where A540 represents the absorbance of the well under study, B is the absorbance of the blank (wells with untreated cells), and C is the absorbance of the control cells (treated with 1% DMSO). The %CV was plotted as a function of the tested concentrations to determine the IC_{50}.

GLIA PRIMARY CELL CULTURE

Astrocytes were kindly provided by Prof. Olivera-Bravo's group and were obtained following the protocol previously reported.[56]

https://doi.org/10.1021/acsomega.5c07982
ACS Omega 2025, 10, 50468−50487

KINASE ENZYMATIC ASSAYS

The $EGFR_{WT}$ enzymatic system kits (catalog number V 3831) and $EGFR_{T790M}$ were obtained from Promega Corporation (Wisconsin, USA). The experiments were conducted following the manufacturer's instructions. For more detailed information, refer to the ADP-Glo Kinase Assay technical manual and the kinase datasheet available at: http://www.promega.com/KESProtocol. Briefly, for the enzymatic reactions, 10-fold serial dilutions of the compounds were prepared from 250 μM to 2.5 × 10^{-4} μM. The reaction mix consisted of 1 μL of the compound dilution (1% DMSO), 2 μL of enzyme (final concentration: 5 ng/μL), and 2 μL of ATP/substrate solution (final concentration: 50 μM/0.2 μg/μL Poly(Glu,Tyr)). Each reaction was performed in triplicate in a 384-well plate with a 1 h incubation at room temperature. The reaction was stopped by adding 5 μL of ADP-Glo postincubation at room temperature for 40 min, followed by the addition of 10 μL of Kinase Detection Reagent. Erlotinib and Osimertinib were used as positive controls for $EGFR_{WT}$ and $EGFR_{T790M}$, respectively. Luminescence was measured after 40 min using a BioTek FLx800 Multi-Detection Microplate Reader (integration time: 0.5−1 s). Data were analyzed by nonlinear regression of normalized results using a least-squares fitting method in GraphPad Prism version 8.0.1 (GraphPad Software, Inc., San Diego, CA, USA).

CELLULAR DEATH MECHANISM STUDIES

A total of 1.5 × 10^4 U-87 MG cells were seeded in p60 plates and maintained in culture for 48 h at 37 °C in a humidified 5% CO_2 atmosphere. Following this incubation period, cells were treated with each test compound and erlotinib at concentrations corresponding to their respective IC_{50} values and further incubated for an additional 24 h. At the end of the treatment, the culture medium was carefully removed and retained for further analysis. Cells were then detached using a cell scraper, ensuring minimal mechanical stress, and collected with the reserved supernatant. The entire suspension was centrifuged at 1500 rpm for 5 min at room temperature. The resulting supernatant was discarded, and the cell pellet was resuspended in 1× PBS and counted using a hemocytometer. Cells were subsequently washed and resuspended in Annexin V binding buffer (10 mM HEPES, 140 mM NaCl, 2.5 mM $CaCl_2$, pH 7.4) at a final concentration of 1.0 × 10^6 cells/mL. To evaluate cell death, an Annexin V/Propidium Iodide (AV/PI) staining assay was performed. Apoptotic cells were identified using Alexa Fluor 488-conjugated Annexin V (3 μL per sample, catalog number A1320), while necrotic cells were marked with Propidium Iodide (PI, 1 mg/mL, final concentration of X μg/mL [add precise value]). Cells were incubated with Annexin V for 30 min in the dark at room temperature. Just prior to flow cytometry analysis, 2 μL of PI were added to each sample. For gating and compensation, unstained cells were used as negative controls, while single-stained cells served as positive controls for each fluorochrome (Annexin V^+/PI^- and Annexin V^-/PI^+ populations). Based on these controls, three distinct cell populations were defined: Annexin V^+/PI^-: Early apoptotic cells; Annexin V^+/PI^+: Late apoptotic cells; Annexin V^-/PI^+: Necrotic cells

Samples were immediately analyzed by flow cytometry, with fluorescence acquisition at 530 nm (FL1) for Annexin V and 630 nm (FL3) for PI. For each condition, fluorescence intensity from 10,000 events was recorded across three independent experiments. Data was processed and analyzed using FlowJo V10.1 software.

***In Vitro* Genetic Toxicity.** The mutagenic potential of compounds (**11**)-(**17**) was evaluated using the Ames test with *Salmonella typhimurium* strains TA97, TA98, TA100, and TA1535, both with (S_9^+) and without (S_9^-) metabolic activation. The maximum nontoxic dose was first determined by incubating TA98 cultures with increasing compound concentrations (up to 500 μg/plate) and assessing bacterial growth on minimal medium plates. For the Ames test, bacterial suspensions were incubated at 37 °C for 1 h with the test compounds in 1× PBS (S_9^-) or S9 mix (S_9^+), followed by plating onto histidine/biotin-supplemented minimal medium and incubation for 48 h. Positive controls included 2-aminoanthracene (2-AA), 2-aminofluorene (2-AF), 4-nitro-*ortho*-phenylenediamine (NPD), and sodium azide (NaN_3), depending on the strain and activation conditions. One % DMSO served as the negative control. Compounds were classified as nonmutagenic, as no dose-dependent increase in revertant colonies was observed, with values consistently below twice the negative control.

Up-and-Down and Biochemical. The oral LD_{50} was determined using the up-and-down procedure, following the OECD recommendations.[57] The limit test was performed with a maximum of five animals administered sequentially, starting with a dose of 2000 mg/kg of body weight, and vital signs were monitored for 72 h using the Irwin test.[58,59] The LD_{50} was calculated using the AOT425StatPgm software.[60] Subsequently, blood was collected from the animals via the orbital sinus and stored in heparinized tubes for later biochemical analysis using a veterinary analyzer (miniRAL, General Panel Rotor MN00001).

pH-Dependent Stability Studies by HPLC Analysis. From a 5 mM stock solution of each compound, working solutions were prepared at a final concentration of 50 μM in three different pH conditions: pH 7.0 (phosphate buffer), pH 8.6 (Tris-HCl buffer), and pH 2.0 (KCl-HCl buffer).[48] To evaluate chemical stability, the solutions were incubated in a water bath at 37 °C for 24 h. Nonincubated solutions and erlotinib were used as controls. Aliquots of 50 μL from each solution were analyzed by HPLC (Agilent 1200, Agilent Technologies, Italy) using a C18 column (Restek, 10 μm, 250 × 4.5 mm). The mobile phase consisted of a gradient of solvent A (water with 0.1% TFA) and solvent B (methanol), with the following program: 0−10 min, 80% B; 10−30 min, 100% B; 30−32 min, 0% B. The absorbance of the eluted peaks was monitored at 335 nm.

Animals. Female BALB/c mice weighing 17−20%g were used, bred and provided by the Unit of Reagents for Experimental Biomodels (URBE), Facultad de Medicina, Universidad de la República, Uruguay. The animals were housed in acrylic cages at 20%; ± %2%°C, under a 12-h light/dark cycle. They were fed *ad libitum* with standard pelleted diet and water and were used after a 5-day acclimation period to the housing conditions. All animal experimental protocols were conducted in accordance with the procedures authorized by the Uruguayan Animal Experimentation Ethics Committee, which previously approved this project (CHEA-UdelaR Protocol No. 240012−000027−22: Protocol No. 1626). All animal experimental protocols followed the principles outlined in the Declaration of Helsinki.

STATISTICAL ANALYSIS

For each analysis, the data was presented as the mean SD. One-way ANOVA statistical analyses were carried out using GraphPad Prism 8.0 software (GraphPad Software Inc.).

https://doi.org/10.1021/acsomega.5c07982
ACS Omega 2025, 10, 50468−50487

IN SILICO APPROACH

Drug-like Properties Prediction. Drug-like properties were calculated using admetQSAR tool kit (http://lmmd.ecust.edu.cn/admetsar1/predict/) from the molecule SMILE code generated with ChemDraw Standard 14.0 software.

Generation of Initial Structures of *closo*-Carborane Compounds Complexed with EGFR Kinase Domain. The structures of *closo*-carborane compounds (**12**, **16** and **17**) were optimized in dichloroethane at the B3LYP-D3/6−31G(d)[61−63] level of theory using the IEF-PCM implicit solvent model[64] implemented in Gaussian 16 Rev. C.01.[65] Then the structures were docked into EGFR kinase domain (taken from the complex with erlotinib, PDB: 1M17)[66] using the AutoDock Vina 1.2.6.[67] For EGFR kinase domain, Gasteiger charges were used while for the aforementioned compounds RESP charges[68] were used. Boron and carbon atoms from the icosahedron were treated as aromatic C atoms since parameters for them are not available in AutoDock Vina 1.2.6.

Molecular Dynamics Simulations. Four systems were considered: the complexes of the EGFR kinase domain with the aforementioned *closo*-carborane compounds and with erlotinib. Structures of the complexes, which were obtained by docking or by X-ray crystallography, were used as starting points. Protonation states of titratable residues were determined with PROPKA 3.0,[69] then tautomerization of histidine residues was determined by visual inspection. Missing hydrogens were added, then complexes were solvated in periodic truncated octahedral boxes of TIP3P water 12 Å around the solute and neutralized using the procedure described by Machado et al.[70] using a salt (KCl) concentration of 0.15 M, using the *leap* utility of AmberTools 24.[71] Systems were subject to energy minimization, heated to 310 K (500 ns of NVT molecular dynamics simulation) and equilibrated at 1.0 atm (1 ns of NPT simulation at 310 K) before running the 300 ns production (NVT, 310 K, 1 atm) simulations. A 10.0 Å cutoff was used to treat direct interactions and long-range interactions were treated using the Particle Mesh Ewald[72] method. For molecular dynamics simulations a 2 fs integration step was used, and bonds involving hydrogen were constrained using the SHAKE algorithm.[73] Temperature was kept by means of the Langevin thermostat,[74] and pressure was kept by means of the Monte Carlo barostat.[75] The *ff14SB* force field was used to describe standard residues, while the *gaff* force field was used to describe ligands (except carborane moiety which was described using parameters developed by Sárosi by et al.[76]). Partial charges of the ligands were obtained using the RESP procedure. Energy minimizations and molecular dynamics simulations were carried out using the *pmemd.cuda* module of AMBER 24.[77] Trajectory analysis was performed using the *cpptraj* module of AmberTools 24.

Binding free energies were estimated using the MM/PBSA and MM/GBSA methods,[78] as implemented in the MMPBSA.py module of *AmberTools24*. Entropic contributions were not included in the calculations.

ASSOCIATED CONTENT

Supporting Information

The Supporting Information is available free of charge at https://pubs.acs.org/doi/10.1021/acsomega.5c07982.

Scheme S1. Screening of reaction conditions for the *N*-alkylation of *ortho*-carboranyl amines (SI_1); Characterization data (^{1}H, ^{13}C, ^{11}B, NMR, HPLC-MS) for compounds (**11**−**17**) (SI_1); Hirshfeld surface analyses and fingerprint plots for compounds (**11**), (**12**), and (**15**), including decomposed d_{norm} maps (SI_1); IC_{50} curves for $EGFR_{WT}$ and $EGFRT_{790M}$ inhibition assays (SI_1); Stability Studies (SI_1); Crystallographic data: fractional atomic coordinates and equivalent isotropic displacement parameters (Tables S2_1a−d), bond distances and angles (Tables S2_2a−d), anisotropic displacement parameters (Tables S2_3a−d), hydrogen atom positions (Tables S2_4a−d), torsion angles (Tables S2_5a−d), and hydrogen-bond distances and angles (Tables S2_6a−d) for compounds **11**−**13** and 15 ((SI_1)); AdmetSAR @ LMMD compounds **11**−**18** (SI_1) (PDF)

AUTHOR INFORMATION

Corresponding Author

Marcos Couto − *Grupo de Química Orgánica Medicinal, Instituto de Química Biológica, Facultad de Ciencias, Universidad de la República, Montevideo 11400, Uruguay; Instituto de Investigación Una Salud, Universidad de la República, Montevideo 11600, Uruguay;* orcid.org/0000-0003-2925-7347; Email: mcouto@fcien.edu.uy

Authors

Belén Dávila − *Grupo de Química Orgánica Medicinal, Instituto de Química Biológica, Facultad de Ciencias, Universidad de la República, Montevideo 11400, Uruguay*

Pablo Vignolo − *Grupo de Química Orgánica Medicinal, Instituto de Química Biológica, Facultad de Ciencias, Universidad de la República, Montevideo 11400, Uruguay*

Ignacio González − *Grupo de Química Orgánica Medicinal, Instituto de Química Biológica, Facultad de Ciencias, Universidad de la República, Montevideo 11400, Uruguay*

Nicole Lecot − *Laboratorio de Técnicas Nucleares Aplicadas a Bioquímica y Biotecnología, Centro de Investigaciones Nucleares, Facultad de Ciencias, Universidad de la República, Montevideo 11400, Uruguay*

Jenner N. Bonanata − *Instituto de Química Biológica, Facultad de Ciencias, Universidad de la República, Montevideo 11400, Uruguay;* orcid.org/0000-0002-3413-8038

María Fernanda García − *Área de Radiofarmacia, Centro de Investigaciones Nucleares, Facultad de Ciencias, Universidad de la República, Montevideo 11400, Uruguay;* orcid.org/0000-0002-2918-5761

Gustavo A. Echeverría − *Departamento de Física, Facultad de Ciencias Exactas, Universidad Nacional de La Plata and Institute IFLP (CONICET, CCT-La Plata), La Plata 1900, Argentina*

Oscar E. Piro − *Departamento de Física, Facultad de Ciencias Exactas, Universidad Nacional de La Plata and Institute IFLP (CONICET, CCT-La Plata), La Plata 1900, Argentina*

Hugo Cerecetto − *Grupo de Química Orgánica Medicinal, Instituto de Química Biológica, Facultad de Ciencias and Área de Radiofarmacia, Centro de Investigaciones Nucleares, Facultad de Ciencias, Universidad de la República, Montevideo 11400, Uruguay; Instituto de Investigación Una Salud, Universidad de la República, Montevideo 11600, Uruguay;* orcid.org/0000-0003-1256-3786

Complete contact information is available at: https://pubs.acs.org/10.1021/acsomega.5c07982

https://doi.org/10.1021/acsomega.5c07982
ACS Omega 2025, 10, 50468−50487

Author Contributions

‡B.D. and P.V. contributed equally. Conceptualization, M.C.; Formal analysis, M.C., H.C.; Investigation: B.D., P.V., I.G., N.L., J.N.B., M.F.G., G.A.E., O.E.P.; Writing-review and editing: M.C., H.C., O.E.P., J.N.B.; Supervision: M.C.; Funding acquisition: M.C., H.C., B.D. All authors have read and agreed to the published version of the manuscript.

Notes

The authors declare no competing financial interest.

■ ACKNOWLEDGMENTS

This work was supported by the Fondo Vaz Ferreira (FVF/2023/484), Dirección Nacional de Innovación, Ciencia y Tecnología (DICYTI), Uruguay; the Comisión Sectorial de Investigación Científica, Universidad de la República, Uruguay (grant 22420230100137UD); and PEDECIBA-Química, Uruguay. M.F.G., N.L., J.N.B., H.C., and M.C. are researchers of the Sistema Nacional de Investigadores-ANII. Additional support was provided by CONICET (PIP 0651) and Universidad Nacional de La Plata (UNLP, Project 11/X857), Argentina. O.E.P. and G.A.E. are Research Fellows of CONICET.

■ ABBREVIATIONS

ADMET,absorption, distribution, metabolism, excretion, and toxicity; BBB,blood−brain barrier; BNCT,boron neutron capture therapy; $(CD_3)_2SO$,deuterated dimethyl sulfoxide; $CDCl_3$,deuterated chloroform; CD_3COCD_3,deuterated acetone; CH_2Cl_2,dichloromethane; DMSO,dimethyl sulfoxide; DMF,*N*,*N*-dimethylformamide; EGFR,epidermal growth factor receptor; Erl,erlotinib; GBM,glioblastoma; H_2SO_4,sulfuric acid; HNO_3,nitric acid; HPLC,high-performance liquid chromatography; HPLC-MS,high-performance liquid chromatography coupled to mass spectrometry; IC_{50},half maximal inhibitory concentration; LD_{50},median lethal dose; mp,melting point; MeOH,methanol; $MgSO_4$,magnesium sulfate; MM/GBSA,molecular mechanics generalized Born surface area; MM/PBSA,molecular mechanics Poisson−Boltzmann surface area; NH_4Cl,ammonium chloride; NH_4OH,Ammonium hydroxide; NMR,nuclear magnetic resonance; OECD,Organisation for Economic Co-operation and Development; ORTEP,Oak Ridge Thermal Ellipsoid Plot Program; PBS,phosphate-buffered saline; RNA-seq,RNA sequencing; SNAr,nucleophilic aromatic substitution; TFA,trifluoroacetic acid; TKR,tyrosine kinase receptor; TLC,thin-layer chromatography

■ REFERENCES

(1) Lima, L.; Barreiro, E. Bioisosterism: A Useful Strategy for Molecular Modification and Drug Design. *Curr. Med. Chem.* **2005**, *12* (1), 23−49.

(2) Meanwell, N. A. Applications of Bioisosteres in the Design of Biologically Active Compounds. *J. Agric. Food Chem.* **2023**, *71* (47), 18087−18122.

(3) Nilova, A.; Campeau, L.-C.; Sherer, E. C.; Stuart, D. R. Analysis of Benzenoid Substitution Patterns in Small Molecule Active Pharmaceutical Ingredients: Miniperspective. *J. Med. Chem.* **2020**, *63* (22), 13389−13396.

(4) Shearer, J.; Castro, J. L.; Lawson, A. D. G.; MacCoss, M.; Taylor, R. D. Rings in Clinical Trials and Drugs: Present and Future. *J. Med. Chem.* **2022**, *65* (13), 8699−8712.

(5) Ritchie, T. J.; Macdonald, S. J. The Impact of Aromatic Ring Count on Compound Developability − Are too many Aromatic Rings a Liability in Drug Design? *Drug Discovery Today* **2009**, *14*, 1011−1020.

(6) Ritchie, T. J.; Macdonald, S. J. Physicochemical Descriptors of Aromatic Character and Their Use in Drug Discovery. *J. Med. Chem.* **2014**, *57*, 7206−7215.

(7) Tse, E. G.; Houston, S. D.; Williams, C. M.; Savage, G. P.; Rendina, L. M.; Hallyburton, I.; Anderson, M.; Sharma, R.; Walker, G. S.; Obach, R. S.; Todd, M. H. Nonclassical Phenyl Bioisosteres as Effective Replacements in a Series of Novel Open-Source Antimalarials. *J. Med. Chem.* **2020**, *63* (20), 11585−11601.

(8) Khanna, I. Drug Discovery in Pharmaceutical Industry: Productivity Challenges and Trends. *Drug Discovery Today* **2012**, *17* (19−20), 1088−1102.

(9) Brown, D. G.; Boström, J. Analysis of Past and Present Synthetic Methodologies on Medicinal Chemistry: Where Have All the New Reactions Gone? *J. Med. Chem.* **2016**, *59* (10), 4443−4458.

(10) Mykhailiuk, P. K. Saturated Bioisosteres of Benzene: Where to Go Next? *Org. Biomol. Chem.* **2019**, *17* (11), 2839−2849.

(11) Marfavi, A.; Kavianpour, P.; Rendina, L. M. Carboranes in Drug Discovery, Chemical Biology and Molecular Imaging. *Nat. Rev. Chem.* **2022**, *6* (7), 486−504.

(12) Grams, R. J.; Santos, W. L.; Scorei, I. R.; Abad-García, A.; Rosenblum, C. A.; Bita, A.; Cerecetto, H.; Viñas, C.; Soriano-Ursúa, M. A. The Rise of Boron-Containing Compounds: Advancements in Synthesis, Medicinal Chemistry, and Emerging Pharmacology. *Chem. Rev.* **2024**, *124* (5), 2441−2511.

(13) Couto, M.; Cerecetto, H. Advancements in the Synthesis and Biological Properties of Carboranes and High-Boron Related Compounds: A Comprehensive Exploration with Emphasis on BNCT Applications. *J. Braz. Chem. Soc.* **2024**, *35*, No. e-20240109.

(14) Scholz, M.; Hey-Hawkins, E. Carbaboranes as Pharmacophores: Properties, Synthesis, and Application Strategies. *Chem. Rev.* **2011**, *111* (11), 7035−7062.

(15) Grimes, R. N. *Carboranes*; Academic Press, Elsevier: Amsterdam and New York, 2016.

(16) Issa, F.; Kassiou, M.; Rendina, L. M. Boron in Drug Discovery: Carboranes as Unique Pharmacophores in Biologically Active Compounds. *Chem. Rev.* **2011**, *111* (9), 5701−5722.

(17) Fitzmaurice, C.; Dicker, D.; Pain, A.; Hamavid, H.; Moradi-Lakeh, M.; MacIntyre, M. F.; Allen, C.; Hansen, G.; Woodbrook, R.; Wolfe, C.; Hamadeh, R. R.; Moore, A.; Werdecker, A.; Gessner, B. D.; Te Ao, B.; McMahon, B.; Karimkhani, C.; Yu, C.; Cooke, G. S.; Schwebel, D. C.; Carpenter, D. O.; Pereira, D. M.; Nash, D.; Kazi, D. S.; De Leo, D.; Plass, D.; Ukwaja, K. N.; Thurston, G. D.; Yun Jin, K.; Simard, E. P.; Mills, E.; Park, E.-K.; Catalá-López, F.; deVeber, G.; Gotay, C.; Khan, G.; Hosgood, H. D., 3rd; Santos, I. S.; Leasher, J. L.; Singh, J.; Leigh, J.; Jonas, J. B.; Sanabria, J.; Beardsley, J.; Jacobsen, K. H.; Takahashi, K.; Franklin, R. C.; Ronfani, L.; Montico, M.; Naldi, L.; Tonelli, M.; Geleijnse, J.; Petzold, M.; Shrime, M. G.; Younis, M.; Yonemoto, N.; Breitborde, N.; Yip, P.; Pourmalek, F.; Lotufo, P. A.; Esteghamati, A.; Hankey, G. J.; Ali, R.; Lunevicius, R.; Malekzadeh, R.; Dellavalle, R.; Weintraub, R.; Lucas, R.; Hay, R.; Rojas-Rueda, D.; Westerman, R.; Sepanlou, S. G.; Nolte, S.; Patten, S.; Weichenthal, S.; Abera, S. F.; Fereshtehnejad, S.-M.; Shiue, I.; Driscoll, T.; Vasankari, T.; Alsharif, U.; Rahimi-Movaghar, V.; Vlassov, V. V.; Marcenes, W. S.; Mekonnen, W.; Melaku, Y. A.; Yano, Y.; Artaman, A.; Campos, I.; MacLachlan, J.; Mueller, U.; Kim, D.; Trillini, M.; Eshrati, B.; Williams, H. C.; Shibuya, K.; Dandona, R.; Murthy, K.; Cowie, B.; Amare, A. T.; Antonio, C. A.; Castañeda-Orjuela, C.; van Gool, C. H.; Violante, F.; Oh, I.-H.; Deribe, K.; Soreide, K.; Knibbs, L.; Kereselidze, M.; Green, M.; Cardenas, R.; Roy, N.; Tillmann, T.; Li, Y.; Krueger, H.; Monasta, L.; Dey, S.; Sheikhbahaei, S.; Hafezi-Nejad, N.; Kumar, G. A.; Sreeramareddy, C. T.; Dandona, L.; Wang, H.; Vollset, S. E.; Mokdad, A.; Salomon, J. A.; Lozano, R.; Vos, T.; Forouzanfar, M.; Lopez, A.; Murray, C.; Naghavi, M.; Global Burden of Disease Cancer Collaboration. The Global Burden of Cancer 2013. *JAMA Oncol.* **2015**, *1* (4), 505−527.

(18) Thapa, R.; Afzal, M.; Goyal, A.; Gupta, G.; Bhat, A. A.; Almalki, W. H.; Kazmi, I.; Alzarea, S. I.; Shahwan, M.; Kukreti, N.; Ali, H.; Dureja, H.; Kumar, P.; Singh, T. G.; Kuppusamy, G.; Singh, S. K.; Dua, K. Exploring ncRNA-Mediated Regulation of EGFR Signalling in

https://doi.org/10.1021/acsomega.5c07982
ACS Omega 2025, 10, 50468−50487

Glioblastoma: From Mechanisms to Therapeutics. *Life Sci.* **2024**, *345*, No. 122613.
(19) Keller, S.; Schmidt, M. H. H. EGFR and EGFRvIII Promote Angiogenesis and Cell Invasion in Glioblastoma: Combination Therapies for an Effective Treatment. *Int. J. Mol. Sci.* **2017**, *18* (6), 1295.
(20) Broniscer, A.; Baker, S. J.; Stewart, C. F.; Merchant, T. E.; Laningham, F. H.; Schaiquevich, P.; Kocak, M.; Morris, E. B.; Endersby, R.; Ellison, D. W.; Gajjar, A. Phase I and Pharmacokinetic Studies of Erlotinib Administered Concurrently with Radiotherapy for Children, Adolescents, and Young Adults with High-Grade Glioma. *Clin. Cancer Res.* **2009**, *15* (2), 701−707.
(21) Griffero, F.; Daga, A.; Marubbi, D.; Capra, M. C.; Melotti, A.; Pattarozzi, A.; Gatti, M.; Bajetto, A.; Porcile, C.; Barbieri, F.; Favoni, R. E.; Lo Casto, M.; Zona, G.; Spaziante, R.; Florio, T.; Corte, G. Different Response of Human Glioma Tumor-Initiating Cells to Epidermal Growth Factor Receptor Kinase Inhibitors. *J. Biol. Chem.* **2009**, *284* (11), 7138−7148.
(22) Karpel-Massler, G.; Halatsch, M.-E. Erlotinib in Glioblastoma − A Current Clinical Perspective. En *Tumors of the Central Nervous System - Primary and Secondary*; InTech, 2014.}.
(23) Prados, M. D.; Chang, S. M.; Butowski, N.; DeBoer, R.; Parvataneni, R.; Carliner, H.; Kabuubi, P.; Ayers-Ringler, J.; Rabbitt, J.; Page, M.; Fedoroff, A.; Sneed, P. K.; Berger, M. S.; McDermott, M. W.; Parsa, A. T.; Vandenberg, S.; James, C. D.; Lamborn, K. R.; Stokoe, D.; Haas-Kogan, D. A. Phase II Study of Erlotinib plus Temozolomide during and after Radiation Therapy in Patients with Newly Diagnosed Glioblastoma Multiforme or Gliosarcoma. *J. Clin. Oncol.* **2009**, *27* (4), 579−584.
(24) Couto, M.; Mastandrea, I.; Cabrera, M.; Cabral, P.; Teixidor, F.; Cerecetto, H.; Viñas, C. Small-Molecule Kinase-Inhibitors-Loaded Boron Cluster as Hybrid Agents for Glioma-Cell-Targeting Therapy. *Chemistry* **2017**, *23* (39), 9233−9238.
(25) Couto, M.; García, M. F.; Alamón, C.; Cabrera, M.; Cabral, P.; Merlino, A.; Teixidor, F.; Cerecetto, H.; Viñas, C. Discovery of Potent EGFR Inhibitors through the Incorporation of a 3D-Aromatic-Boron-Rich-Cluster into the 4-Anilinoquinazoline Scaffold: Potential Drugs for Glioma Treatment. *Chemistry* **2018**, *24* (13), 3122−3126.
(26) Couto, M.; Alamón, C.; Sánchez, C.; Dávila, B.; Fernández, M.; Lecot, N.; Cabral, P.; Teixidor, F.; Viñas, C.; Cerecetto, H. Carboranylanilinoquinazoline EGFR-inhibitors: Toward "lead-to-candidate" stage in the drug-development pipeline. *Fut. Med. Chem.* **2019**, *11*, 2273−2285.
(27) Alamón, C.; Dávila, B.; Cerecetto, H.; Couto, M. Exploring the Cell Death Mechanisms of Cytotoxic [1,2,3]Triazolylcarborane Lead Compounds against U87 MG Human Glioblastoma Cells. *Chem. Biol. Drug Des.* **2023**, *101* (6), 1435−1445.
(28) Alamón, C.; Dávila, B.; García, M. F.; Nievas, S.; Dagrosa, M. A.; Thorp, S.; Kovacs, M.; Trias, E.; Faccio, R.; Gabay, M.; Zeineh, N.; Weizman, A.; Teixidor, F.; Viñas, C.; Gavish, M.; Cerecetto, H.; Couto, M. A Potential Boron Neutron Capture Therapy Agent Selectively Suppresses High-Grade Glioma. In Vitro and in Vivo Exploration. *Mol. Pharmaceutics* **2023**, *20* (5), 2702−2713.
(29) Useini, L.; Mojić, M.; Laube, M.; Lönnecke, P.; Dahme, J.; Sárosi, M. B.; Mijatović, S.; Maksimović-Ivanić, D.; Pietzsch, J.; Hey-Hawkins, E. Carboranyl Analogues of Mefenamic Acid and Their Biological Evaluation. *ACS omega* **2022**, *7* (28), 24282−24291.
(30) Useini, L.; Mojić, M.; Laube, M.; Lönnecke, P.; Mijatović, S.; Maksimović-Ivanić, D.; Pietzsch, J.; Hey-Hawkins, E. Carborane Analogues of Fenoprofen Exhibit Improved Antitumor Activity. *ChemMedChem.* **2023**, *18* (5), No. e202200583.
(31) Stockmann, P.; Kuhnert, L.; Leinung, W.; Lakoma, C.; Scholz, B.; Paskas, S.; Mijatović, S.; Maksimović-Ivanić, D.; Honscha, W.; Hey-Hawkins, E. The More the Better-Investigation of Polymethoxylated N-Carboranyl Quinazolines as Novel Hybrid Breast Cancer Resistance Protein Inhibitors. *Pharmaceutics* **2023**, *15* (1), No. 241.
(32) Selg, C.; Gordić, V.; Krajnović, T.; Buzharevski, A.; Laube, M.; Kazimir, A.; Lönnecke, P.; Wolniewicz, M.; Sárosi, M. B.; Schädlich, J.; Pietzsch, J.; Mijatović, S.; Maksimović-Ivanić, D.; Hey-Hawkins, E. Re-Design and Evaluation of Diclofenac-Based Carborane-Substituted Prodrugs and Their Anti-Cancer Potential. *Sci. Rep.* **2024**, *14* (1), 30488.
(33) Couto, M.; Alamón, C.; Nievas, S.; Perona, M.; Dagrosa, M. A.; Teixidor, F.; Cabral, P.; Viñas, C.; Cerecetto, H. Bimodal Therapeutic Agents against Glioblastoma, One of the Most Lethal Forms of Cancer. *Chemistry* **2020**, *26* (63), 14335−14340.
(34) Saadeh, F. S.; Mahfouz, R.; Assi, H. I. EGFR as a clinical marker in glioblastomas and other gliomas. *International Journal of Biological Markers* **2018**, *33* (1), 22−32.
(35) Zhang, J.; Antonyak, M. A.; Singh, G.; Cerione, R. A. A Mechanism for the Upregulation of EGF Receptor Levels in Glioblastomas. *Cell Rep.* **2013**, *3* (6), 2008−2020.
(36) Kugler, M.; Nekvinda, J.; Holub, J.; El Anwar, S.; Das, V.; Šícha, V.; Pospíšilová, K.; Fábry, M.; Král, V.; Brynda, J.; Kašička, V.; Hajdúch, M.; Řezáčová, P.; Grüner, B. Inhibitors of CA IX Enzyme Based on Polyhedral Boron Compounds. *Chembiochem* **2021**, *22* (18), 2741−2761.
(37) OECD. *Test No. 471: Bacterial Reverse Mutation Test*; OECD, **2020**.
(38) OECD. *Test No. 423: Acute Oral Toxicity - Acute Toxic Class Method*; OECD, **2002**.
(39) *BALB/c Mouse Biochemistry and Hematology: North American Colonies*; Charles River, 2008.
(40) Cheng, F.; Li, W.; Zhou, Y.; Shen, J.; Wu, Z.; Liu, G.; Lee, P. W.; Tang, Y. admetSAR: A Comprehensive Source and Free Tool for Assessment of Chemical ADMET Properties. *J. Chem. Inf. Model.* **2012**, *52* (11), 3099−3105.
(41) Shen, J.; Cheng, F.; Xu, Y.; Li, W.; Tang, Y. Estimation of ADME Properties with Substructure Pattern Recognition. *J. Chem. Inf. Model.* **2010**, *50* (6), 1034−1041.
(42) Pham The, H.; González-Álvarez, I.; Bermejo, M.; Mangas Sanjuan, V.; Centelles, I.; Garrigues, T. M.; Cabrera-Pérez, M. Á. Silico prediction of Caco-2 cell permeability by a classification QSAR approach. *Mol. Inf* **2011**, *30*, 376−385.
(43) Kido, Y.; Matsson, P.; Giacomini, K. M. Profiling of a Prescription Drug Library for Potential Renal Drug-Drug Interactions Mediated by the Organic Cation Transporter 2. *J. Med. Chem.* **2011**, *54* (13), 4548−4558.
(44) Carbon-Mangels, M.; Hutter, M. C. Selecting relevant descriptors for classification by Bayesian estimates: a comparison with decision trees and support vector machines approaches for disparate datasets. *Mol. Inf* **2011**, *30*, 885−895.
(45) Marchese Robinson, R. L.; Glen, R. C.; Mitchell, J. B. O. Development and Comparison of hERG Blocker Classifiers: Assessment on Different Datasets Yields Markedly Different Results. *Mol. Inform.* **2011**, *30* (5), 443−458.
(46) Wang, S.; Li, Y.; Wang, J.; Chen, L.; Zhang, L.; Yu, H.; Hou, T. ADMET Evaluation in Drug Discovery. 12. Development of Binary Classification Models for Prediction of hERG Potassium Channel Blockage. *Mol. Pharmaceutics* **2012**, *9* (4), 996−1010.
(47) Lagunin, A.; Filimonov, D.; Zakharov, A.; Xie, W.; Huang, Y.; Zhu, F.; Shen, T.; Yao, J.; Poroikov, V. Computer-aided Prediction of Rodent Carcinogenicity by PASS and CISOC-PSCT. *QSAR Comb. Sci.* **2009**, *28* (8), 806−810.
(48) Couto, M.; Ovalle, S. d.; Cabrera, M.; Cerecetto, H.; González, M. Searching Phase II Enzymes Inducers, from Michael Acceptor-[1,2]Dithiolethione Hybrids, as Cancer Chemopreventive Agents. *Future Med. Chem.* **2015**, *7* (7), 857−871.
(49) *CrysAlisPro, Rigaku Oxford Diffraction*, version 1.171.38.41; Rigaku Coorporation, (**2015**).
(50) Sheldrick, G. M. SHELXT - Integrated Space-Group and Crystal-Structure Determination. *Acta Crystallogr. A Found. Adv.* **2015**, *71* (Pt 1), 3−8.
(51) Sheldrick, G. M. A Short History of SHELX. *Acta Crystallogr. A* **2008**, *64* (Pt 1), 112−122.
(52) van der Sluis; A. L. Spek, P. BYPASS: an effective method for the refinement of crystal structures containing disordered solvent regions. *Found. Crystallogr* **1990**, *A46*, 194−201.

https://doi.org/10.1021/acsomega.5c07982
ACS Omega 2025, 10, 50468−50487

(53) Spek, A. L. PLATON SQUEEZE: A Tool for the Calculation of the Disordered Solvent Contribution to the Calculated Structure Factors. *Acta Crystallogr. C Struct. Chem.* **2015**, *71* (Pt 1), 9−18.
(54) Spackman, M. A.; Jayatilaka, D. Hirshfeld surface analysis. *CrystEngComm* **2009**, *11*, 19−32.
(55) Spackman, P. R.; Turner, M. J.; McKinnon, J. J.; Wolff, S. K.; Grimwood, D. J.; Jayatilaka, D.; Spackman, M. A. CrystalExplorer: a program for Hirshfeld surface analysis, visualization and quantitative analysis of molecular crystals. *J. Appl. Crystallogr.* **2021**, *54* (3), 1006−1011.
(56) Olivera-Bravo, S.; Bolatto, C.; Otero Damianovich, G.; Stancov, M.; Cerri, S.; Rodríguez, P.; Boragno, D.; Hernández Mir, K.; Cuitiño, M. N.; Larrambebere, F.; Isasi, E.; Alem, D.; Canclini, L.; Marco, M.; Davyt, D.; Díaz-Amarilla, P. Neuroprotective Effects of Violacein in a Model of Inherited Amyotrophic Lateral Sclerosis. *Sci. Rep.* **2022**, *12* (1), 4439.
(57) OECD Guidelines for the Testing of Chemicals, Section 4: *Test No. 425: Acute Oral Toxicity: Up-and- Down Procedure*; OECD publishing, **2008**.
(58) Irwin, S. Comprehensive observational assessment: Ia. A systematic, quantitative procedure for assessing the behavioral and physiologic state of the mouse. *Psychopharmacologia* **1968**, *13*, 222−257.
(59) Roux, S.; Sablé, E.; Porsolt, R. D. Primary Observation (Irwin) Test in Rodents for Assessing Acute Toxicity of a Test Agent and Its Effects on Behavior and Physiological Function. *Curr. Protoc. Pharmacol.* **2005**, *27* (1), 10.
(60) OECD. *Section 4: Software. Software to be Used with TG 425*; OECD.
(61) Becke, A. D. Density-Functional Thermochemistry. III. The Role of Exact Exchange. *J. Chem. Phys.* **1993**, *98* (7), 5648−5652.
(62) Grimme, S.; Antony, J.; Ehrlich, S.; Krieg, H. A Consistent and AccurateAb InitioParametrization of Density Functional Dispersion Correction (DFT-D) for the 94 Elements H-Pu. *J. Chem. Phys.* **2010**, *132* (15), No. 154104.
(63) Francl, M. M.; Pietro, W. J.; Hehre, W. J.; Binkley, J. S.; Gordon, M. S.; DeFrees, D. J.; Pople, J. A. Self-Consistent Molecular Orbital Methods. XXIII. A Polarization-Type Basis Set for Second-Row Elements. *J. Chem. Phys.* **1982**, *77* (7), 3654−3665.
(64) Tomasi, J.; Mennucci, B.; Cammi, R. Quantum Mechanical Continuum Solvation Models. *Chem. Rev.* **2005**, *105* (8), 2999−3094.
(65) Frisch, M. J.; Trucks, G. W.; Schlegel, H. B.; Scuseria, G. E.; Robb, M. A.; Cheeseman, J. R.; Scalmani, G.; Barone, V.; Petersson, G. A.; Nakatsuji, H.; Li, X.; Caricato, M.; Marenich, A. V.; Bloino, J.; Janesko, B. G.; Gomperts, R.; Mennucci, B.; Hratchian, H. P.; Ortiz, J. V.; Izmaylov, A. F.; Sonnenberg, J. L.; Williams-Young, D.; Ding, F.; Lipparini, F.; Egidi, F.; Goings, J.; Peng, B.; Petrone, A.; Henderson, T.; Ranasinghe, D.; Zakrzewski, V. G.; Gao, J.; Rega, N.; Zheng, G.; Liang, W.; Hada, M.; Ehara, M.; Toyota, K.; Fukuda, R.; Hasegawa, J.; Ishida, M.; Nakajima, T.; Honda, Y.; Kitao, O.; Nakai, H.; Vreven, T.; Throssell, K.; Montgomery, Jr., J. A.; Peralta, J. E.; Ogliaro, F.; Bearpark, M. J.; Heyd, J. J.; Brothers, E. N.; Kudin, K. N.; Staroverov, V. N.; Keith, T. A.; Kobayashi, R.; Normand, J.; Raghavachari, K.; Rendell, A. P.; Burant, J. C.; Iyengar, S. S.; Tomasi, J.; Cossi, M.; Millam, J. M.; Klene, M.; Adamo, C.; Cammi, R.; Ochterski, J. W.; Martin, R. L.; Morokuma, K.; Farkas, O.; Foresman, J. B.; Fox, D. J. *Gaussian, Inc., Wallingford CT (2016) GaussView 5.0*; Gaussian Inc.: Wallingford, E.U.A..
(66) Stamos, J.; Sliwkowski, M. X.; Eigenbrot, C. Structure of the Epidermal Growth Factor Receptor Kinase Domain Alone and in Complex with a 4-Anilinoquinazoline Inhibitor. *J. Biol. Chem.* **2002**, *277* (48), 46265−46272.
(67) Eberhardt, J.; Santos-Martins, D.; Tillack, A. F.; Forli, S. AutoDock Vina 1.2.0: New Docking Methods, Expanded Force Field, and Python Bindings. *J. Chem. Inf. Model.* **2021**, *61* (8), 3891−3898.
(68) Cieplak, P.; Cornell, W. D.; Bayly, C.; Kollman, P. A. Application of the Multimolecule and Multiconformational RESP Methodology to Biopolymers: Charge Derivation for DNA, RNA, and Proteins. *J. Comput. Chem.* **1995**, *16* (11), 1357−1377.
(69) Søndergaard, C. R.; Olsson, M. H. M.; Rostkowski, M.; Jensen, J. H. Improved Treatment of Ligands and Coupling Effects in Empirical Calculation and Rationalization of pKa Values. *J. Chem. Theory Comput.* **2011**, *7* (7), 2284−2295.
(70) Machado, M. R.; Pantano, S. Split the Charge Difference in Two! A Rule of Thumb for Adding Proper Amounts of Ions in MD Simulations. *J. Chem. Theory Comput.* **2020**, *16* (3), 1367−1372.
(71) Case, D. A.; Aktulga, H. M.; Belfon, K.; Cerutti, D. S.; Cisneros, G. A.; Cruzeiro, V. W. D.; Forouzesh, N.; Giese, T. J.; Götz, A. W.; Gohlke, H.; Izadi, S.; Kasavajhala, K.; Kaymak, M. C.; King, E.; Kurtzman, T.; Lee, T.-S.; Li, P.; Liu, J.; Luchko, T.; Luo, R.; Manathunga, M.; Machado, M. R.; Nguyen, H. M.; O'Hearn, K. A.; Onufriev, A. V.; Pan, F.; Pantano, S.; Qi, R.; Rahnamoun, A.; Risheh, A.; Schott-Verdugo, S.; Shajan, A.; Swails, J.; Wang, J.; Wei, H.; Wu, X.; Wu, Y.; Zhang, S.; Zhao, S.; Zhu, Q.; Cheatham, T. E., III; Roe, D. R.; Roitberg, A.; Simmerling, C.; York, D. M.; Nagan, M. C.; Merz, K. M., Jr. AmberTools. *J. Chem. Inf. Model.* **2023**, *63* (20), 6183−6191.
(72) Darden, T.; York, D.; Pedersen, L. Particle Mesh Ewald: An N·log(N) Method for Ewald Sums in Large Systems. *J. Chem. Phys.* **1993**, *98* (12), 10089−10092.
(73) Ryckaert, J.-P.; Ciccotti, G.; Berendsen, H. J. C. Numerical Integration of the Cartesian Equations of Motion of a System with Constraints: Molecular Dynamics of n-Alkanes. *J. Comput. Phys.* **1977**, *23* (3), 327−341.
(74) Loncharich, R. J.; Brooks, B. R.; Pastor, R. W. Langevin Dynamics of Peptides: The Frictional Dependence of Isomerization Rates of N-acetylalanyl-N′-methylamide. *Biopolymers* **1992**, *32* (5), 523−535.
(75) Åqvist, J.; Wennerström, P.; Nervall, M.; Bjelic, S.; Brandsdal, B. O. Molecular Dynamics Simulations of Water and Biomolecules with a Monte Carlo Constant Pressure Algorithm. *Chem. Phys. Lett.* **2004**, *384* (4−6), 288−294.
(76) Sárosi, M.-B.; Lybrand, T. P. Molecular Dynamics Simulation of Cyclooxygenase-2 Complexes with Indomethacin Closo-Carborane Analogs. *J. Chem. Inf. Model.* **2018**, *58* (9), 1990−1999.
(77) Case, D. A.; Aktulga, H. M.; Belfon, K.; Ben-Shalom, I. Y.; Cheatham, T. E. I.; Cisneros, G. A.; Cruzeiro, V. W. D.; Darden, T. A.; Forouzesh, N.; Ghazimirsaeed, M.; Girambasu, G.; Giese, T. J.; Gilson, M. K.; Gohlke, H.; Goetz, A. W.; Harris, J.; Huang, Z.; Izadi, S.; Izmaylov, A. F.; Kasavajhala, K.; Kaymak, M. C.; Kolossváry, I.; Kovalenko, A.; Kurtzman, T.; Lee, T.-S.; Li, P.; Li, Z.; Lin, C.; Liu, J.; Luchko, T.; Luo, R.; Machado, M. R.; Manathunga, M.; Merz, K. M., Jr.; Miao, Y.; Mikhailovskii, O.; Monard, G.; Nguyen, H. M.; O'Hearn, K. A.; Onufriev, A. V.; Pan, F.; Pantano, S.; Rahnamoun, A.; Roe, D. R.; Roitberg, A.; Sagui, C.; Wang, J.; Wang, J.; Wu, X.; Wu, Y.; Xiong, Y.; Xue, Y.; York, D. M.; Zhao, C.; Zhu, Q.; Kollman, P. A. *AMBER 2024*.
(78) Genheden, S.; Ryde, U. Methods to Estimate Ligand-Binding Affinities. *Expert Opinion on Drug Discovery* **2015**, *10* (5), 449−461.

https://doi.org/10.1021/acsomega.5c07982
ACS Omega 2025, 10, 50468−50487